

1 **On the automatic and *a priori* design of unstructured mesh resolution**
2 **for coastal ocean circulation models**

3 **Keith J. Roberts¹, William J. Pringle^{1*}, Joannes J. Westerink¹, Marite Teresa Contreras¹,**
4 **Damrongsak Wirasaet¹**

5 ¹Department of Civil and Environmental Engineering and Earth Sciences, University of Notre
6 Dame, Notre Dame, IN

7 **Key Points:**

- 8 • The U.S. East Coast and Gulf Coast domain is automatically discretized with a 50-m mini-
9 mum mesh size.
- 10 • *A priori* mesh size functions based on shoreline geometry and seabed topography are used.
- 11 • A sequence of mesh designs systemically analyze the response of surface tides to mesh size
12 distribution.
- 13 • Recommendations of mesh size function combinations and parameters to efficiently and ac-
14 curately discretize the domain are presented.

*

Corresponding author: William Pringle, wpringle@nd.edu

Abstract

This study investigates the design of unstructured mesh resolution and its impact on the modeling of barotropic tides along the United States East Coast and Gulf Coast (ECGC). A discrete representation of a computational ocean domain (mesh design) is necessary due to finite computational resources and an incomplete knowledge of the physical system (e.g., shoreline and seabed topography). The selection of mesh resolution impacts both the numerical truncation error and the approximation of the system's physical domain. To increase confidence in the design of high-resolution coastal ocean meshes and to quantify the efficacy of current mesh design practices, an automated mesh generation approach is applied to objectively control resolution placement based on *a priori* information such as shoreline geometry and seabed topographic features. The simulated harmonic tidal elevations for each mesh design are compared to that of a reference solution, computed on a 10.8 million vertex mesh of the ECGC region with a minimum shoreline resolution of 50-m. Our key findings indicate that existing mesh designs that use uniform resolution along the shoreline and slowly varying resolution sizes on the continental shelf inefficiently discretize the computational domain. Instead, a targeted approach that places fine resolution in narrow geometric features, along steep topographic gradients, and along pronounced submerged estuarine channels, while aggressively relaxing resolution elsewhere, leads to a mesh with an order of magnitude fewer vertices than the reference solution with comparable accuracy (within 3% harmonic elevation amplitudes in 99% of the domain).

1 Introduction and background

Two-dimensional (2D) unstructured triangular meshes are widely used to represent the horizontal domain in the simulation of hydrodynamic processes of ocean, shelf and inland coastal water systems. In general, these variable resolution meshes are used to study a broad spectrum of processes in the coastal ocean from wind waves with periods on the order of seconds to large scale shelf and oceanic circulation with timescales on the order of days to months. Most commonly, barotropically-driven long wave processes (tides, surge, and tsunami) with periods on the order of minutes to hours are simulated with these meshes. This includes the modeling of tidal dynamics [Blanton *et al.*, 2004; Chen *et al.*, 2011; Pringle *et al.*, 2018a] and the prediction of extreme water levels during high energy events such as tropical and extratropical storms [Westerink *et al.*, 2008; Dietrich *et al.*, 2010, 2011; Beardsley *et al.*, 2013; Chen *et al.*, 2013; Hope *et al.*, 2013; Xu *et al.*, 2013; Zheng *et al.*, 2013; Xie *et al.*, 2016; Cyriac *et al.*, 2018]. Critically, unstructured triangular meshes facilitate seamless cross-scale modeling of the complete long wave spectrum [Zhang and Baptista, 2008; Zhang *et al.*, 2016; Pringle *et al.*, 2019].

Unstructured meshes are used to capture the detailed hydrodynamic response driven by the governing physical processes and their interactions with the physical system. Historically in fluid mechanics, approaches to mesh design and adaption have often been based on *a posteriori* techniques based on the residual of the flow solution on a per element basis [e.g. Oden *et al.*, 1990; Behrens, 1998]. In coastal modeling, an *a posteriori* analysis has been performed using a formal local truncation error analysis [LTEA; Hagen *et al.*, 2000, 2002; Parrish and Hagen, 2009] with the objective to equalize the truncation error throughout the computational domain. However, as finer mesh sizes are used to reduce the truncation error, new narrower shoreline details emerge that can alter the system's response and these aspects are difficult to incorporate into the error indicator. Thus, while the estimate of the numerical truncation error for a given initial mesh description can be minimized, the system domain error may persist because critical features still do not exist in the boundary description and these features may not be detectable by the error indicator.

The aforementioned considerations motivates us to use a feature-driven *a priori* approach. In fact, for the most part meshes for coastal modeling have been developed using an *a priori* approach adjusting resolution to match both the physical system's length scale and estimated length scales of the dominant physics [e.g., Lyard *et al.*, 2006; Bunya *et al.*, 2010; Chen *et al.*, 2011; Luettich and Westerink, 2013; Kerr *et al.*, 2013; Chen *et al.*, 2016]. Feature-driven *a priori* approaches have been proposed to automatically design meshes in this manner [Bilgili *et al.*, 2006; Conroy *et al.*,

2012; Roberts et al., 2018]. Nevertheless, until now it has been difficult to build a sufficient number of meshes to enable a controlled comparison of the simulated results for realistic coastal ocean hydrodynamic models through the traditional *ad hoc* and tedious [Hagen et al., 2001] development process. However, recent advances in automated unstructured mesh generation technology for the ocean [Remacle and Lambrechts, 2016; Engwirda, 2017; Candy and Pietrzak, 2018; Avdis et al., 2018; Roberts et al., 2018] now enable well-defined repeatable workflows for generating detailed multiscale coastal ocean meshes. These approaches alleviate the burden previously associated with the model development steps and ensure that the development process is sufficiently controlled to facilitate inter-comparisons between simulation results from a variety of mesh designs with logical perturbations.

A ubiquitous feature-driven *a priori* meshing criteria for coastal modeling is the wavelength-to-gridscale heuristic that sizes resolution according to an estimate of depth-dependent shallow water wave celerity to maintain constant discretization of the wavelength of the dominant mode [Westerink et al., 1994; Lyard et al., 2006; Greenberg et al., 2007; Westerink et al., 2008]. This heuristic produces meshes that contain the finest resolution nearshore, element size transitions that vary smoothly, and nearly constant resolution across the continental shelf. However, the wavelength-to-gridscale heuristic is based on a one-dimensional analysis that assumes no bathymetric gradients and thus cannot capture complexity of seabed features like shelf breaks and isolated banks [Greenberg et al., 2007] nor the intricacies of the 2D shoreline. Further, submarine channels that are important to convey flow into the estuarine system can become coarsely discretized with its application. While a long legacy of meshes have been built with this heuristic, the application of resolution using this approach leads to models with many degrees-of-freedom if the parameter dictating the number of nodes per wavelength is set to a large value to compensate for inadequately targeting resolution at the aforementioned features.

Consideration of the topographic-length scale, i.e., applying finer resolution directly proportional to the seabed depth and inversely proportional to seabed topographic gradient has also been widely conducted [Lyard et al., 2006; Chen et al., 2016; Engwirda, 2017]. This approach refines the resolution in proximity to the shelf break and submarine ridges and banks, which often tend to be co-located with large gradients in the solution [Hannah and Wright, 1995]. In fact, the LTEA analysis method proposed by Hagen et al. [2000, 2002] demonstrated that the minimization of truncation error tended to produce a distribution of vertices that resembled the application of the topographic-length scale. Representing steep gradients is also useful to capture submarine ridges and rough topography over which internal tides are generated [Garrett and Kunze, 2007]. This process is often included as a parameterized dissipation process in barotropic tidal models [Green and Nycander, 2013; Pringle et al., 2018a,b]. However, a drawback of the topographic-length scale is that on the inner shelf the topographic gradient to depth ratio can become large due to topographic irregularities which leads to excessively fine resolution as compared to the length scales of the dominant physics.

Unstructured meshes have a powerful capability to efficiently capture the geometrically complex form of the shoreline and of the complex estuaries and the connected dendritic inland channels, but most prior works have not taken full advantage of this capability by applying uniformly fine resolution along shorelines and within inland waterways in regions of interest. For instance, NOMAD (NOAA Operational Model with ADCIRC), a mesh used for real-time predictions of storm surge and tides (e.g., ASGS [Fleming et al., 2008]), uses uniform coastal resolution of approximately 250 m along all the United States East Coast and Gulf Coasts (ECGC) [Technology Riverside Inc. and AECOM, 2015]. Other examples of meshes that resolve the shoreline uniformly includes those used in recent long-term regional analyses of storm surge and tides in ECGC [\sim 1-5 km; Muis et al., 2019; Marsooli and Lin, 2018], and those used for hurricane-induced coastal flooding in the northern Gulf of Mexico [\sim 100 m; Kerr et al., 2013]. On one hand, uniform shoreline resolution ensures that the representation of the inlet/backbay system that control coastal inshore hydrodynamics is best represented in the mesh of the specified resolution. On the other hand, the application of nearly uniform resolution nearshore over-resolves many sections of the coastline and inland waters that are straight and geometrically simple leading to a situation where cost con-

119 straits then necessitate under-resolving narrow and constricted waterways. Studies in the South
 120 Atlantic Bight have demonstrated that the representation of the estuary system as a whole can al-
 121 ter the morphodynamic feedback between the tides and the shoreline form [Blanton *et al.*, 2004;
 122 Bacopoulos and Hagen, 2017]. Thus, beyond applying fine resolution zones nearshore, it is often
 123 critical to resolve the intricate dendritic inland waters and to quantify the feedback effects from the
 124 integrated system. These irregular shoreline and inland systems can be efficiently captured using
 125 highly variable mesh resolution.

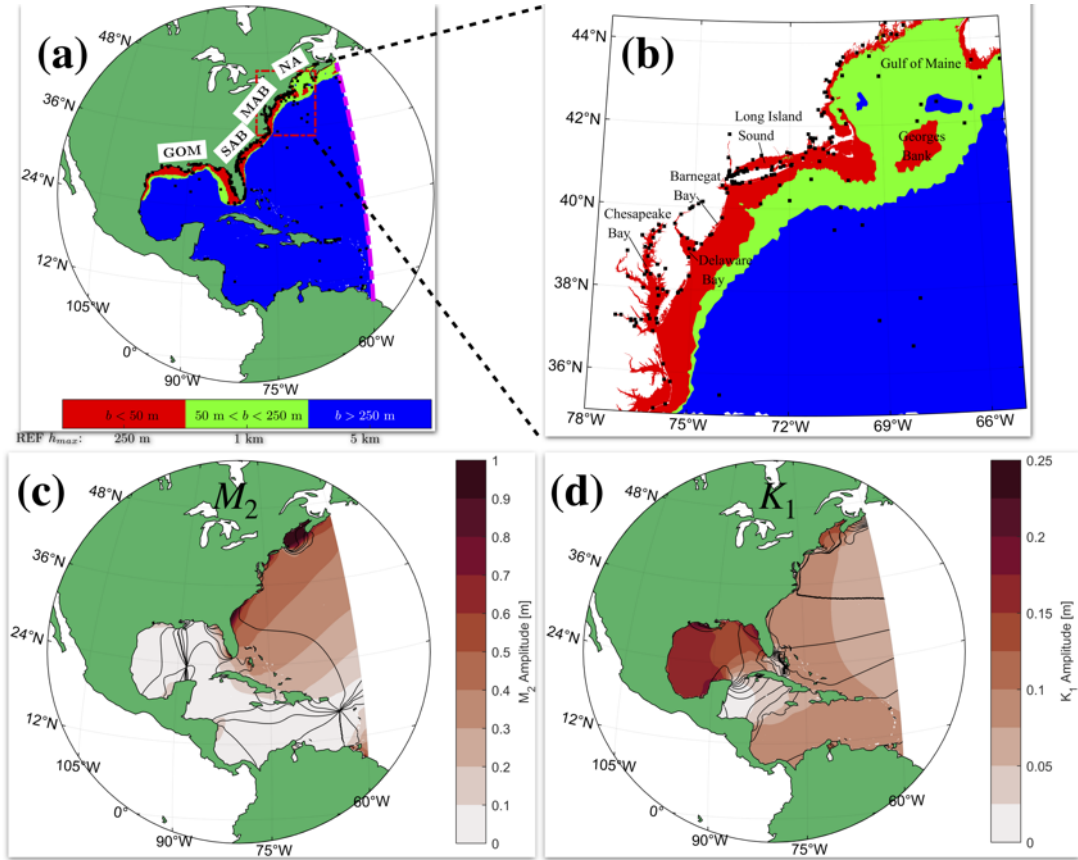
126 Another consideration for developing unstructured meshes is the rate of element size transi-
 127 tions between zones of variable resolution otherwise referred to as the gradation [Persson, 2006]. It
 128 is known that element size transitions must be smooth and bounded above by a constant to avoid
 129 numerical errors and inaccuracies [Shewchuk, 2002; Bilgili *et al.*, 2006]. In fact, the error analysis
 130 undertaken by Hagen *et al.* [2000] clearly demonstrates that a gradation above 50% will cause odd
 131 order error terms to dominate and subsequently degrade a formally second order numerical method
 132 to first order. While a theoretical upper bound value for the gradation is known, the total number
 133 of vertices in a coastal ocean discretization can wildly vary depending on the choice of gradation
 134 below 50% (a large gradation will lead to fewer vertices). Thus, the gradation rate needs to be ex-
 135 plored to identify a suggested tighter range of values that efficiently discretizes the physical domain
 136 while maintaining accuracy in the simulation of the coastal ocean.

137 A common first step in the production of a coastal hydrodynamic model is to assess the sim-
 138 ulated accuracy of astronomical tides [e.g., Pringle *et al.*, 2018a] prior to the simulation of extreme
 139 sea levels. At this initial stage of the model development process, the model is calibrated through
 140 adjustments to frictional and dissipative parameterizations in order to agree with measured data.
 141 However, when the mesh underresolves shoreline and seabed features, the system's response may
 142 become distorted leading to an inability to correctly produce solutions across the entire domain
 143 and energy spectrum. An example of this would be tuning the model to agree with observations of
 144 dominant semi-diurnal elevation tidal constituent regionally but this may not lead to a good agree-
 145 ment globally nor for the other tidal constituents. Instead, by gathering knowledge on how tidal
 146 solution depends on mesh resolution in realistic coastal modeling problems, we can enable efficient
 147 and uniformly more accurate mesh designs that can then facilitate more dynamically correct cali-
 148 brations of friction parameterizations.

149 Our premise is that the numerical modeling of the circulation and flow of water is largely
 150 driven and controlled by the representation of the physical system and the representation of the
 151 physical system is integrally related to the mesh sizing functions. Thus, the sizing functions need
 152 to be carefully considered for ensuring high fidelity coastal ocean hydrodynamic simulations that
 153 have a relatively low associated computational cost. This is particularly relevant for operational/real-
 154 time forecast systems in order to be practically computationally feasible. Many of the previously
 155 used *a priori* mesh size heuristics (e.g., topographic-length scale, and distance-to-shoreline) have
 156 proven useful in practice for producing accurate solutions for tides and storm surges. Thus, we
 157 have devised an approach that combines and builds on such mesh size heuristics to variably resolve
 158 shoreline geometry, seabed topography, controlling the geometric expansion of element sizes, and
 159 capturing submarine channels that convey flow into and out of the estuaries. Our ultimate goal is
 160 to capture the physical system and response with the fewest number of degrees of freedom while
 161 preserving the performance of the solution compared to measured data. Here, we apply our ap-
 162 proach to the widely studied ECGC region and conduct an in-depth analysis of the sensitivity of
 163 the barotropic tides to the domain discretization.

164 This paper addresses the following two questions:

- 165 a) How does the simulation of barotropic tides respond to the representation of shoreline ge-
 166 ometry and seabed topography in the ECGC region? What are the sources of error and how
 167 do these contribute to the measured differences?
- 168 b) Can we incorporate our results from a) to make recommendations for a set of mesh size
 169 functions that place resolution according to shoreline geometry and seabed topography to



180 **Figure 1.** The study area in which colored zones in the top panels indicate the mesh size upper bounds (h_{max}) in
 181 the reference (REF) mesh (minimum mesh size is $L_{min} = 50$ m). The red and green colored zones together indicate
 182 the comparison zones for all the cumulative area fraction error curve calculations. The dashed magenta line indicates
 183 the open ocean boundary on which tidal elevations are specified. The bottom left and right panels indicate TPXO9.1
 184 solutions of the M_2 and K_1 tidal constituent elevation amplitudes (colors) and phase contours in intervals of 30° (M_2)
 185 and 15° (K_1).

170 efficiently discretize coastal ocean domains that approximately reproduce simulation results
 171 from an extremely well-resolved mesh?

172 2 Methods, Data and Tools

173 2.1 ECGC Study Domain and Data

174 The ECGC study domain for this work (Figure 1) contains a single open ocean boundary
 175 along the 60° W meridian which is placed here for geometric simplicity and because it lies in the
 176 deep ocean where the tides vary gradually and hence suitable for coupling to global tidal model
 177 solutions that are highly accurate in the deep ocean [Stammer *et al.*, 2014]. The placement of the
 178 open boundary in this way is sufficiently far from the coastal zones to represent tide responses
 179 throughout the ECGC domain [Westerink *et al.*, 1994].

186 The domain is classified into four distinct regions as shown in Figure 1 along with co-tidal
 187 and co-amplitude lines of the dominant constituents. The tides are predominately semi-diurnal
 188 dominated by the M_2 along the Eastern Coast of the United States – North Atlantic (NA), Mid-
 189 Atlantic Bight (MAB), and South Atlantic Bight (SAB). In the western half of the Gulf of Mexico

(GOM) the K_1 and O_1 dominate water level variations, while the eastern side is mixed-diurnal with the M_2 , K_1 , O_1 , and S_2 contributing roughly in equal parts.

2.1.1 Bathymetric and Shoreline Datasets

The bathymetric data used for this study are primarily based on SRTM15+ [Sandwell *et al.*, 2014] and supplemented in areas of overlap with the Coastal Relief Model [CRM; Amante and Eakins, 2009] in addition to local 1/3 and 1/9 arc-sec NCEI topo-bathymetric coastal elevation model datasets where available (<https://www.ngdc.noaa.gov/mgg/coastal/coastal.html>). The entire bathymetric dataset was integrated into a final digital elevation model (DEM) that was re-sampled on a uniform grid spacing of 3 arc-sec (~ 90 m), which is equal to the resolution of the CRM. For SRTM15+ and the CRM, the vertical uncertainty in the data is generally larger than the discrepancy between local mean sea level and the NAVD88 vertical reference datums, so no effort was made to rectify the vertical datum for these data. However, all NCEI local and regional datasets were adjusted to local mean sea level using VDatum [White and Hess, 2016] where the transformation was available. The horizontal datum of the re-sampled DEM is in geographic coordinates or WGS84.

Since the shoreline (where land meets the ocean in the temporal mean sense) as it exists in nature has a fractal geometry and is constantly evolving due to sedimentation and erosional processes, variations in discharge, sea level rise, and anthropomorphic effects, its exact representation may be intractable. For the purposes of this work, we consider a static version of the shoreline as depicted from the relatively recent (5-10 years old) topo-bathymetric data used in this study. A polyline that approximates the local mean sea level shoreline was extracted using the GRASS Geographical Information Systems `r.contour` module with a cut parameter of 150 [GRASS Development Team, 2017]. While higher quality shoreline vector datasets exist, a preference was given to the shoreline extracted from the re-sampled DEM that was created for this work given that it would produce mesh boundaries that are aligned with the 0-m contour from the data sources. In other words, this helps to improve the agreement with the location of where the shoreline is when topo-bathymetric data is interpolated onto the mesh vertices. The discrete shoreline extracted from the DEM model can only resolve shoreline length-scales down to its horizontal resolution of 3 arc-sec (approximately 90 m).

2.1.2 Tide Gauge Data

Harmonic tidal constituent observations at tide gauges in ECGC (Figure 1) are used in this study to validate the model simulations on selected meshes. The observations are predominantly made up of posted harmonic constituents at 636 National Oceanic and Atmospheric Administration (NOAA) coastal tide gauges (<https://tidesandcurrents.noaa.gov/stations.html?type=Harmonic+Constituents>). An additional 31 observations located on the continental shelf and in deep water [Stammer *et al.*, 2014] are also included (available from <ftp://ftp.legos.obs-mip.fr/pub/FES2012-project/data/gauges/2013-12-16/>).

2.2 Hydrodynamic Model Configuration

This study uses the ADvanced CIRCulation model (ADCIRC) [Luettich and Westerink, 2004; Westerink *et al.*, 2008] to perform the hydrodynamic simulations of two-dimensional (2D) barotropic tides. ADCIRC is a continuous-Galerkin finite element model that solves the primitive continuity equation using the so-called Generalized Wave Continuity Equation [GWCE; Lynch and Gray, 1979; Kinnmark, 1988] and a depth-averaged momentum equation on an unstructured triangular mesh [Westerink *et al.*, 1992]. It is formally a second-order solver that discretizes the domain with linear elements.

We perform all simulations with the following setup: the model is forced by astronomical tidal elevation open ocean boundary conditions, astronomical tidal equilibrium potential terms, and astronomical tidal self-attraction and loading (SAL) terms [Hendershott, 1972].

238 In the ADCIRC solver, the time and space advective components of the equations can be
 239 excluded from calculations for numerical stability purposes; however, all terms were included in
 240 the calculations. Further wetting/drying was enabled although a minimum depth is enforced on the
 241 shoreline of 1 m below sea level to ensure flow through narrow channels on the scale of the min-
 242 imum resolution. A constant quadratic bottom friction was used with the standard coefficient of
 243 0.0025. Horizontal dissipation was parameterized through a constant lateral eddy viscosity term of
 244 $50 \text{ m}^2\text{s}^{-1}$. The GWCE mass matrix is solved using an explicit time discretization with mass lump-
 245 ing instead of the consistent implicit method. This choice was not found to affect the simulation
 246 results at the 2 second simulation timesteps we are using here with the Courant-limited explicit
 247 timestepping scheme. Therefore, the explicit method was preferred due to improved computation-
 248 ally efficiency (approximately twice as fast) [Tanaka et al., 2011].

249 2.3 Mesh Generation

250 The construction of regional coastal ocean meshes for hydrodynamic simulations in mod-
 251 els such as ADCIRC is an involved process with many degrees of variation. In order to analyze
 252 how mesh resolution may affect numerical simulations, it is vital to have an automated and repro-
 253 ducible workflow to systematically control aspects of the mesh design. By reproducible we mean
 254 that given the exact same inputs and options, the vertex locations of a new instance of the mesh
 255 will be approximately the same having vertex/elemental densities within a fraction of the target
 256 density function and leading to negligible differences between simulation results repeated on vari-
 257 ous instances of the mesh. The approximate similarity of meshes is evidenced in results throughout
 258 the manuscript: nearly similar mesh designs exhibit the smallest relative differences between their
 259 solutions.

260 Some approaches and tools have been developed recently to make these workflows feasible
 261 [Engwirda, 2017; Gorman et al., 2008; Candy and Pietrzak, 2018; Roberts et al., 2018]. For this
 262 work, all unstructured meshes were developed with the *OceanMesh2D* software [Roberts et al.,
 263 2018; Roberts and Pringle, 2018]. *OceanMesh2D* is a self-contained MATLAB mesh generation
 264 toolkit for the development of 2D unstructured triangular meshes. Specifically, we use Version 2.0
 265 of the software which is an extension of V1.0 [Roberts et al., 2018] with support for mesh gener-
 266 ation using map projections to ensure that meshes on the sphere conform to Earth’s curvature and
 267 obey user-defined resolution requests which are specified in meters. Any map projection that is
 268 featured in the *m_map* mapping package [Pawlowicz, 2018] can be selected.

269 A number of meshes are automatically generated in Lambert conformal conic projection
 270 space using the multiscale meshing approach [Roberts et al., 2018], whereby multiple boxes are
 271 used to cover the region roughly indicated by the green and red colored zones in Figure 1(a)-(b).
 272 Inside these boxes, the minimum resolution L_{min} is specified to between 50 m and 250 m, depend-
 273 ing on the experiment (see Section 2.4). A larger box covering the whole study region is used to
 274 mesh the rest of the domain with a minimum resolution of 1 km that is placed uniformly along
 275 the shoreline. The result is one seamless unstructured mesh, in which the software automatically
 276 smooths mesh resolution sizes between regions.

277 Topo-bathymetric data, available on a structured grid (DEM), is interpolated onto the mesh
 278 vertices using the grid-scale averaging approach that is built into the mesh generation software
 279 [Roberts et al., 2018]. Grid-scale averaging is used to minimize aliasing of the seabed topography
 280 on the mesh vertices that would otherwise arise from curve-fitting interpolation schemes (e.g., linear
 281 interpolation). The minimization of sub-grid scale topo-bathymetric features in the interpolated
 282 seabed topography is important in order to study the effect of mesh resolution on the solution.

283 2.4 Experimental Design

284 In Sections 3.1 to 3.4 five experiments are explored to examine the effects of targeted place-
 285 ment of mesh resolution at various seabed and shoreline features according to a mesh size function
 286 or constraint (Table 1). Within each experiment three meshes (categorized as ‘fine’, ‘medium’, and

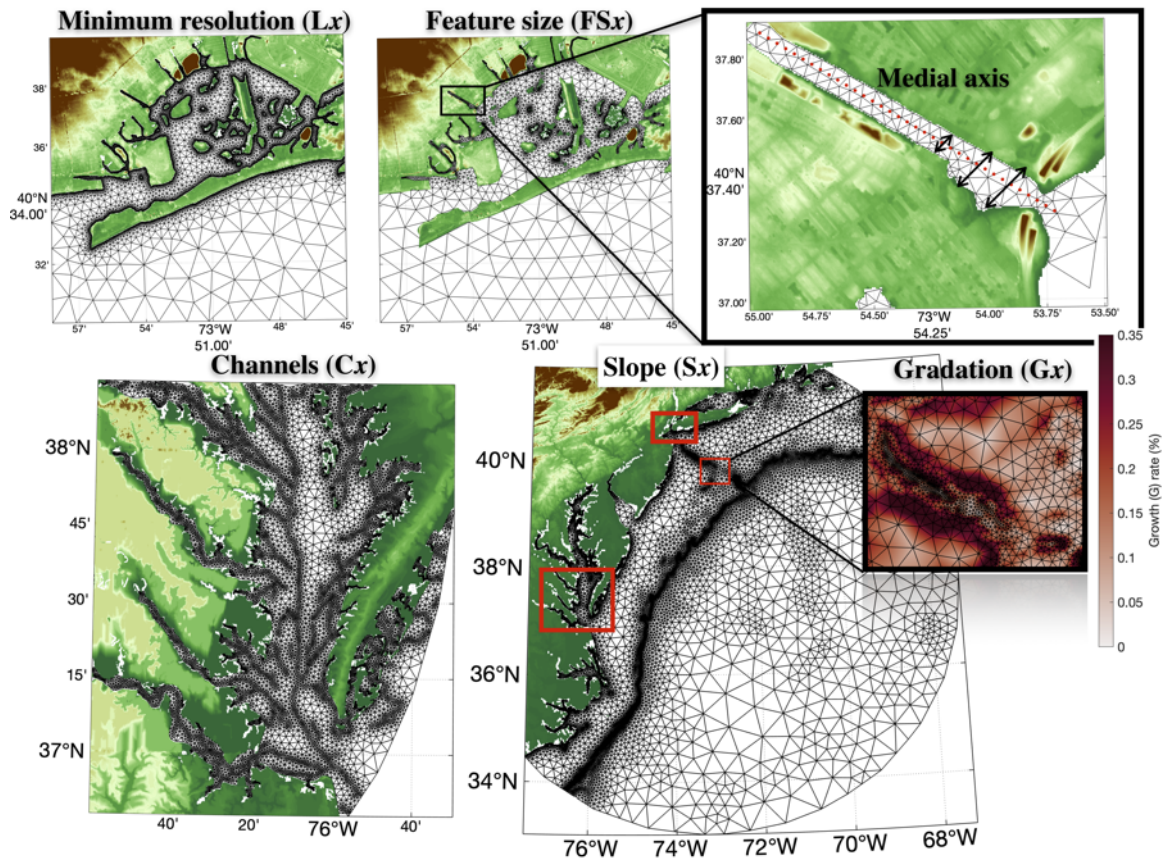
‘coarse’ resolution) are generated by varying a single mesh size function parameter while holding all other parameters constant. Note that the variation of mesh sizing parameters is a multi-faceted problem and all the parameters interact (e.g., one parameter’s value can mask effects of another). For example, a relatively higher feature size may cause finer resolution in deep offshore features that can be largely influential on the simulation of tides, as later shown. All meshes require a minimum mesh size and an element-to-element mesh size gradation rate (henceforth referred to as gradation), which are set to 50-m uniformly along the shoreline and 15%, respectively, unless otherwise stated. The maximum mesh size is set to 10 km for all meshes.

The effect of the mesh size functions on the resulting triangulation’s that are used in the various experiments (Table 1) are graphically illustrated in Figure 2, and described below:

- In the *distance* function (Figure 2(a)), mesh resolution is dictated by the minimum mesh size at the shoreline (L_{min}) and the maximum allowable expansion rate (g). The variation of L_{min} forms Experiment 1.
- The *feature size* function (Figure 2(b)) places mesh resolution according to the width of the geometric feature. The width is estimated as two times the sum of the distance from a point in the computational domain to the nearest shoreline point plus the distance from the same point to the nearest medial axis (Figure 2(c)). Varying the number of elements per geometric feature width forms Experiment 2.
- The *gradation* function bounds the mesh size transitions on the structured grid that the mesh size function is calculated on, which will determine the gradation (g) on the mesh’s triangulation. The variation of this parameter only forms Experiment 3.
- The *slope* function (Figure 2(e)) places mesh resolution according to the length of a topographic feature, targeting regions of high topographic gradients such as the continental shelf break and slope. Experiment 4 varies the number of elements per topographic length-scale.
- The *submarine channel* function (Figure 2(d)) targets mesh resolution along and near well-defined submarine channels such as dredged shipping channels or morphodynamic conveyances within estuaries that are identified through an upslope area calculation using a 1,000 DEM cell minimum threshold in Geographical Information Systems software. Experiment 5 varies the number of elements per channel width. The channel width is estimated according to the seabed depth near the channel and an assumed slope angle of 30° with the seabed floor [see *Roberts and Pringle, 2018*].

A highly-refined reference (REF) mesh (Table 1) was generated to act as a proxy for the ‘true’ solution against which our meshes in the experiments are compared. In this mesh, a set of depth-based maximum element size constraints were used and a mesh size gradation of 15%. Specifically, the minimum mesh resolution is 50-m and the maximum resolution was bounded above by 250 m nearshore (depth, $b < 50$ m), 1 km on the continental shelf ($50 \text{ m} < b < 250$ m), and 5 km in the deep ocean ($b > 250$ m). These mesh size constraints are conservative and they represent values that could be accommodated in terms of the total computational cost, Courant-based stability constraint, and the resolution of the geospatial data used (~ 90 m). The REF mesh contains $N = 10,746,955$ vertices and represents a mesh design that we classify as ‘overly-discretized’ in the sense that as this study will later demonstrate, it is possible to substantially reduce the vertex count while maintaining solution accuracy. It is important to note that for all mesh configurations the REF mesh is indeed finer than the other mesh designs except for the S20 mesh design in a local region on the Western side of the GOM.

Each mesh was used to perform a 122-day tidal simulation to assess the effects on the astronomical tides due to variations in mesh design. In these simulations, ADCIRC is forced through the tidal equilibrium potential and SAL terms throughout the domain and at the open ocean boundaries with four major semi-diurnal (M_2 , N_2 , S_2 , K_2) and four major diurnal tidal constituents (K_1 , O_1 , P_1 , Q_1). Open boundary elevations are obtained from TPXO9.1 (<http://volkov.oce.orst.edu/tides/global.html>) tidal solutions; SAL terms are obtained from FES2014 tidal loading solutions (<ftp://ftp.legos.obs-mip.fr/pub/FES2012-project/data/LSA/FES2014/>). In the assessment of the results of these simulations, a focus is placed primarily on the variation in the major semi-diurnal



320 **Figure 2.** An illustration of the five mesh size functions that were investigated in and around the Mid-Atlantic Bight
 321 region along the Eastern United States coastline. Seabed topography is colored and relevant quantities are noted in the
 322 text.

318 **Table 1.** The five experiments explored each containing three meshes in which the variable mesh size function param-
 319 eter is indicated by x . The properties of the finely-resolved REF mesh used for a baseline comparison is also shown.

Experiments	Meshes			Mesh Size Function [m]	L_{min} [m]	L_{max} [km]	g [%]
	Fine	Medium	Coarse				
1: Minimum Mesh Size	L50	L150	L250	$Lx = x + 0.15d_s$	x	10	15
2: Feature Size	FS8	FS4	FS2	$FSx = 2 * \frac{(d_s + d_m)}{x}$	50	10	15
3: Grade	G15	G25	G35	$Gx \Rightarrow 100 \left \frac{L_i - L_j}{X_i - X_j} \right < x$	50	10	x
4: Slope	S20	S10	S5	$Sx = \frac{2\pi}{x} \frac{b}{ \nabla b }$	50	10	15
5: Submarine channels	C1.0	C0.5	C0.1	$Cx = \frac{2\pi}{x} \frac{b}{\tan(30^\circ)}$	50	10	35
Reference (REF)	-	-	-	REF = $50 + 0.15d_s$	50	0.25 : $b < 50$ m 1 : $b < 250$ m 5 : $b > 250$ m	15

L_{min} : minimum mesh size
 L_{max} : maximum mesh size
 L_i : mesh size at i defined by the circumradius of each triangle
 X_i : coordinate of i on grid to compute edgelengths
 i and j : adjacent elements
 g : gradation
 d_s : shortest distance to the shoreline
 d_m : shortest distance to the medial axis
 b : topo-bathymetric depth (positive below sea level)
 ∇ : gradient operator

344 tide (M_2) since this is the predominant tidal constituent along the ECGC. The major diurnal tide
 345 (K_1) is also included where relevant.

346 The tidal elevations are decomposed into harmonic constituents using a least-squares method
 347 at all points within the domain. Relative errors (RE) in harmonic tidal elevation amplitudes from
 348 all sequences of experiments are calculated by linearly interpolating the solution from the REF
 349 mesh onto the experiment under consideration, subtracting the solutions, and then normalizing by
 350 REF, i.e.,

$$RE = \frac{A_{ID} - A_{REF}}{A_{REF}} \times 100[\%] \quad (1)$$

351 where A is the harmonic elevation amplitude of the tidal constituent in the experiment (ID) and
 352 the REF meshes. A focus is placed on the M_2 and K_1 elevation amplitudes as these represent the
 353 predominant semi-diurnal and diurnal constituents in the ECGC domain (Section 2.1).

354 The calculation of the RE is proceeded in this manner to keep data extrapolation to a mini-
 355 mum so that the same shoreline geometric complexity as depicted in each mesh is present in both
 356 solutions under comparison. For all differences, statistics are only performed on vertices in which
 357 the absolute difference from REF exceeds 1 mm or the RE between solutions is greater than 0.1%.
 358 These significance values are considered sufficiently small to ignore for the modeling purposes of
 359 barotropic tides along the ECGC, which have magnitudes on the order of centimeters to meters.

360 The convergence characteristics of the experiments are examined by comparing the cumu-
 361 lative area fraction errors (CAFE) of the RE statistic along the continental shelf margins of the
 362 ECGC region ($b < 250$ m) where high mesh resolution zones were deployed (i.e., union of the
 363 green and red colored zones in Figure 1). To be consistent throughout, CAFE curves only consider
 364 errors ($A_{ID} - A_{REF}$) that exceed 1 mm or feature a RE greater than 0.1%. On these CAFE plots,

365 the y-axis value of a point falling on these curves indicates the percent area having a difference
 366 greater (less) than the positive (negative) value on the x-axis. A solution that has “converged” in-
 367 dicates that 99% of the comparison region has a $\pm 5\%$ RE. This definition of convergence may be
 368 arbitrary but it represents a statistic that can enable a consistent comparison between solutions and
 369 a more stringent accuracy standard than currently set by the U.S. COASTAL Act¹.

370 Last, in Section 3.5 we summarize the experiments through the standard deviation of the
 371 variation in the RE statistics from the REF mesh. Further, the contribution of numerical error ver-
 372 sus error in the physical approximation of the domain is illustrated. Finally, based on the results
 373 of the five experiments described above we generate mesh designs that combine mesh size func-
 374 tions/experiments together to create a mesh with fewer vertices that can approximately mimic the
 375 tidal solution accuracy of the REF mesh.

376 The following set of statistics are computed to compare the accuracy, in terms of error against
 377 tide gauge observations (Section 2.1.2), of the simulated tidal solutions between the REF mesh and
 378 the combination mesh designs.

$$E = \left(0.5 \left[A_o^2 + A_m^2 - 2A_o A_m \cos(\theta_o - \theta_m) \right] \right)^{1/2} \quad (2)$$

$$B = \frac{\sum_{t=1}^T (E_{ID} - E_{REF})}{\sum_{t=1}^T E_{REF}} \quad (3)$$

$$\gamma^2 = \frac{\text{var}(E_{ID} - E_{REF})}{\text{var}(E_{REF})} \quad (4)$$

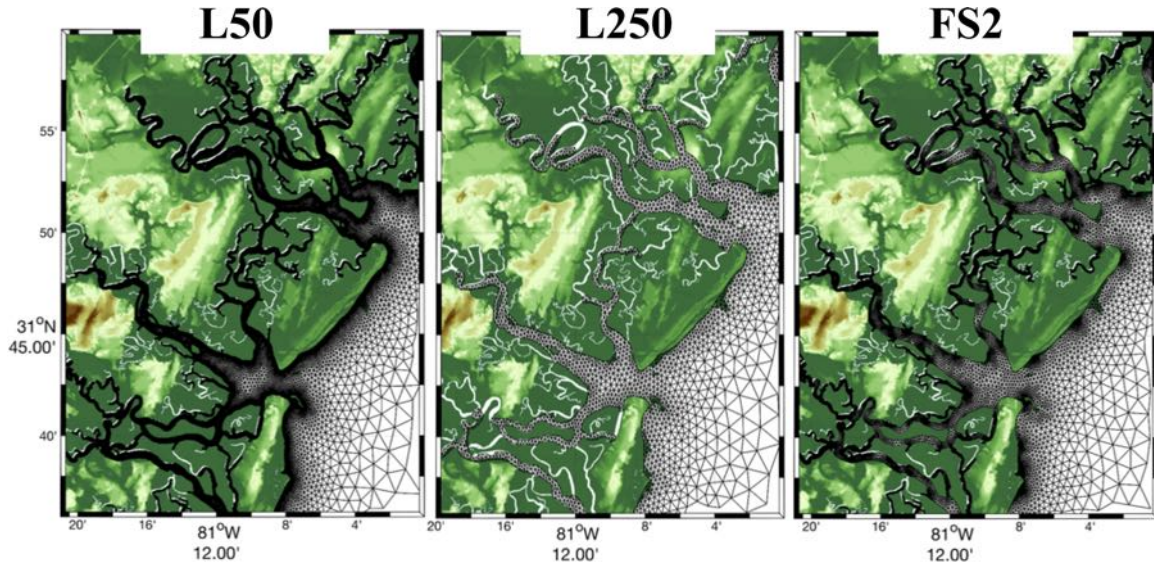
379 where E is the complex root-mean-square error of a tidal constituent for one cycle and account
 380 for the amplitude and phase errors, A and θ are the amplitudes and phase lags of the tidal con-
 381 stituent respectively, the subscripts ‘o’ and ‘m’ refer to the observed and modeled values respec-
 382 tively, and T in the sum is the total number of tide gauges. B is the normalized mean bias and γ^2
 383 is the normalized variance (*var*) of the discrepancies of E between the REF mesh and a particular
 384 mesh combination (ID). A positive value of B indicates that the mesh combination has on average
 385 greater values of E than REF, while a negative bias indicates the model is outperforming the REF
 386 solution. The smaller the value of γ^2 , the more similar the mesh’s solution is to REF in terms of
 387 the distribution of E . Since, a model can be tuned to fit observations locally, such as by employing
 388 variable bottom friction coefficients in regions where errors arise, the main aim here is to minimize
 389 γ^2 and B , through the effects of mesh resolution on the solution under the assumption that REF is
 390 sufficiently resolved. For reference, the REF solution has a median E for the M_2 of 3.9 cm (com-
 391 puted on all 667 tide gauges, Section 2.1.2).

392 **3 Results**

393 **3.1 Resolving the shoreline**

394 The representation of the shoreline determines the simulated accuracy in modeling the phys-
 395 ical interaction between forcing agents (e.g., tides, winds, and waves) with shoreline geometri-
 396 cal features (e.g., coves, headlands, back-bays, and lagoons). From a modeling standpoint, the
 397 shoreline’s representation must be simplified to satisfy computational resources by removing fine-
 398 shoreline details from the mesh’s boundary description that are smaller than the minimum mesh
 399 resolution. However, when the shoreline is simplified, it alters the approximation of the physical
 400 domain, and hence possibly the system’s tidal response [e.g., *Molines et al.*, 1989; *Greenberg et al.*,
 401 2007].

¹ <https://www.weather.gov/sti/coastalact>



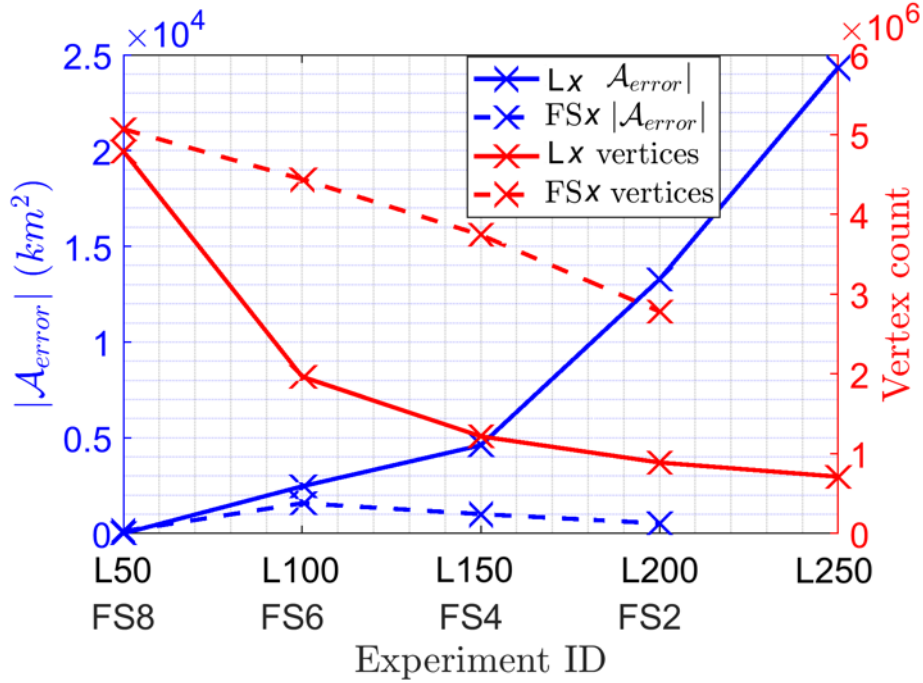
425 **Figure 3.** Mesh connectivity near Ossabaw Island, Georgia that illustrates changes to the capturing of narrow channel
 426 geometries as minimum mesh resolution is increased from 50 m (left) to 250 m (middle), and when using a shoreline
 427 width function that varies minimum mesh resolution between 50 m and 250 m (right) automatically based on shoreline
 428 geometric properties.

402 This section uses the results from Experiments 1 (Lx) and 2 (FSx) to explore the effects of
 403 varying a specified minimum resolution at the shoreline and of varying shoreline resolution accord-
 404 ing to a feature size estimation, respectively. A comparative example of the Lx and FSx designs
 405 along an estuarine region is illustrated in Figure 3. As the minimum mesh resolution is coarsened
 406 from 50 m to 250 m, narrow waterways, tributaries, and estuaries that are smaller in horizontal
 407 length-scale than the minimum mesh resolution are automatically removed in the mesh genera-
 408 tion process [Roberts *et al.*, 2018]. The removal of fine-scale shoreline geometry is considered a
 409 shoreline approximation error in the sense that the approximate representation of the shoreline de-
 410 parts from its representation in the original shoreline dataset. In contrast, the feature size approach
 411 creates a mesh that represents the physical system accurately by connecting small waterways to-
 412 gether in a similar manner to L50, but requiring fewer vertices as resolution can expand in size
 413 away from geometric constrictions along the shoreline (Figure 3).

414 It is important to note that the variation in the minimum element size along the shoreline will
 415 impact the sizing of elements near and along adjacent inner and outer shelf seabed topographical
 416 features as all the meshes are graded to expand in element size offshore. In addition, the appli-
 417 cation of the FSx will lead to finer resolution near more irregular shoreline features. Considering
 418 this, more pronounced differences in element sizes will tend to occur between FSx and Lx in prox-
 419 imity to shoreline segments that are highly irregular in their form. Thus, besides the obvious im-
 420 pact on the representation of the shoreline via either the Lx or FSx design, the variations in this
 421 experiment also implicitly alter the representation of the inner and outer shelf seabed topographic
 422 gradients.

423 The shoreline approximation error is quantified by integrating the area enclosed by the polyg-
 424 onal region that defines the mesh boundary (S in which the sub-script denotes the experiment ID).

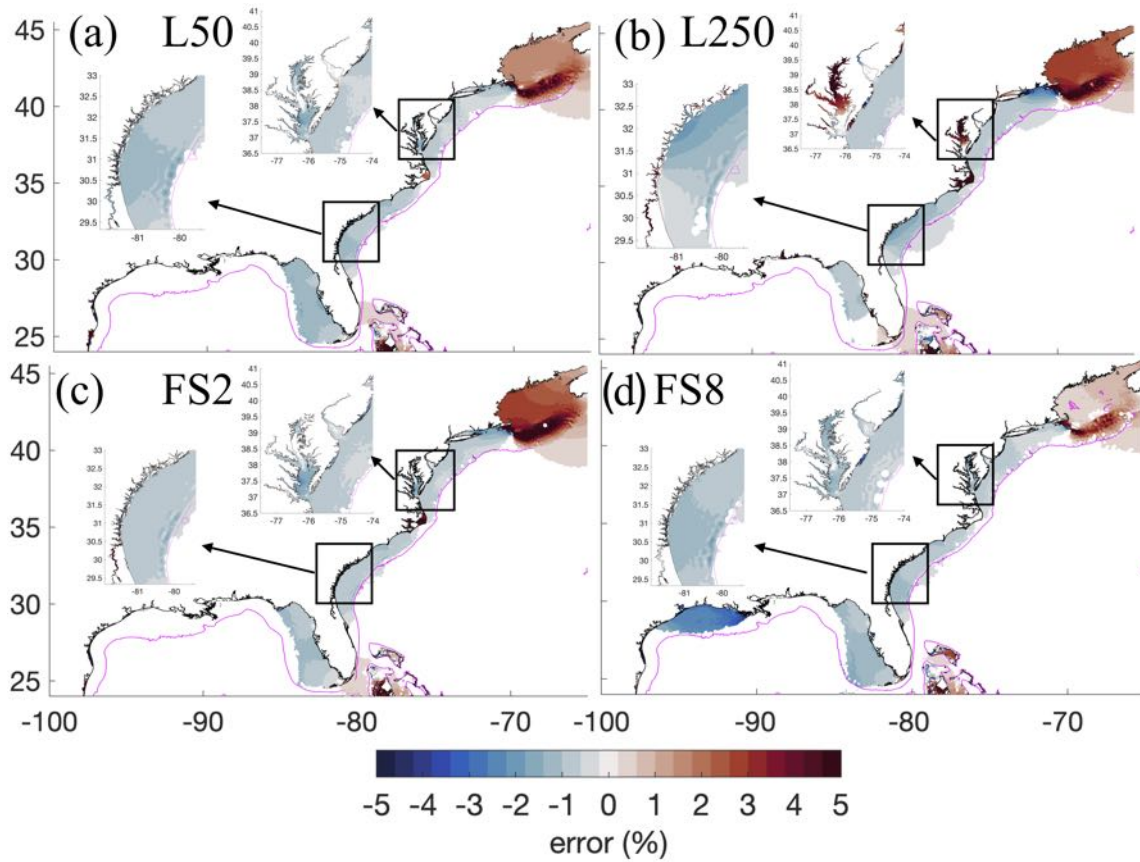
$$\mathcal{A}_{error} = |S_{ID} - S_{Ref}| \quad (5)$$



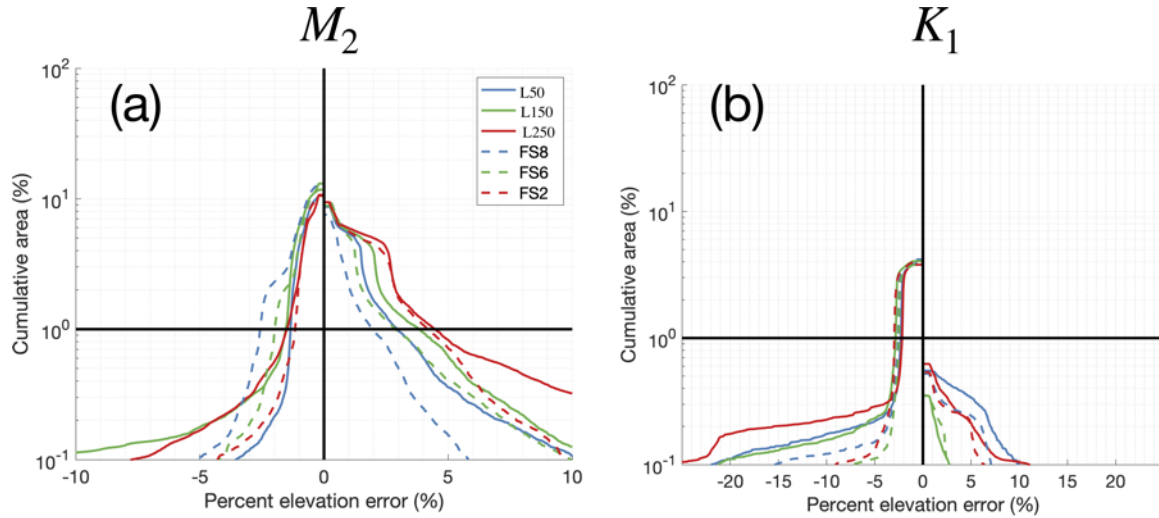
429 **Figure 4.** The shoreline geometry error \mathcal{A}_{error} , Equation (5), on the left axis for the meshes used in the shoreline
 430 approximation experiment along with the total vertex count for each mesh on the right axis. Solid lines represent data
 431 for meshes created with uniform shoreline resolution Lx and dashed lines indicate meshes created with the feature size
 432 approach FSx.

437 \mathcal{A}_{error} increases geometrically as the minimum shoreline resolution is coarsened from 50 m to
 438 250 m in the Lx meshes (Figure 4). For example, $\mathcal{A}_{error} = 2,200 \text{ km}^2$ for L100 increases approx-
 439 imately ten-fold to $\mathcal{A}_{error} = 22,000 \text{ km}^2$ for L250, while the total vertex count reduces from 4.9
 440 million to 0.8 million vertices between L250 and L50 mesh designs. In contrast, the FSx experi-
 441 ments exhibits no correspondence between total vertex counts and shoreline approximation error
 442 and \mathcal{A}_{error} remains small reaching a maximum of approximately $1,500 \text{ km}^2$. The FSx design dis-
 443 tributes 50-m mesh sizes in narrow waterways and along high curvature shoreline sections, while
 444 allowing mesh sizes to expand up to 250 m along straighter shoreline segments. The predominate
 445 variation in vertex counts in the FSx design is the number of vertices per geometric width of the
 446 shoreline, not the minimum element size. Thus, the FS2 design is capable of preserving a similar
 447 amount of shoreline geometry as L50 (e.g., Figure 3a,c) but with approximately two times fewer
 448 vertices.

449 As is evident in Figure 5, the variation in the representation of the shoreline predominately
 450 affects the M_2 elevation amplitude in shallow shelf regions ($< 250\text{-m}$ depth range). A largely in-
 451 significant error ($< 1 \text{ mm}$ or $\pm 0.1\%$) was observed in the K_1 elevation amplitude (not shown).
 452 The relative M_2 errors (RE) among the Lx experiments are greatest for L250 and smallest for L50
 453 (Figure 5a-b), demonstrating the improvement of finer resolution. Large RE values are concen-
 454 trated in estuaries in the SAB and in the MAB around the Chesapeake Bay and the Gulf of Maine
 455 where large RE values of 10-15% are found in the L250 mesh (Figure 5b). In the MAB, SAB, and
 456 eastern GOM shelf zones, there is a weak 1-3% deamplification in the M_2 amplitude with the ex-
 457 ception of the Chesapeake Bay estuary, which exhibits a pronounced RE of +5-10% as the mesh
 458 resolution is coarsened from L50 to L250. In general, the FSx meshes (Figure 5c-d) produce sim-
 459 ilar relative error patterns to the Lx meshes. However, negative RE values are only $< 1\%$ in the
 460 Chesapeake and SAB for the coarsest Lx design (FS2) compared to RE values in L250 which are



433 **Figure 5.** Panels (a)-(b) depict the relative error in the M_2 harmonic elevation amplitude from the REF solution
 434 when the minimum mesh resolution along the shoreline is coarsened from 50 m and 250 m. Panels (c)-(d) depicts the
 435 relative error (RE) in the M_2 harmonic elevation amplitude from solutions computed on meshes built with the feature
 436 size function. Insets around areas described in more detail are shown.



477 **Figure 6.** The cumulative area fraction error (CAFE) from the REF solution in the comparison region for panel (a)
 478 the M_2 elevation amplitude and panel (b) the K_1 elevation amplitude. The dotted lines denotes solutions computed on
 479 meshes that use the FSx design while the solid-lines denote meshes created with the L_x design.

461 approximately $\pm 3\%$ here. Further, FS2 reduces the amplification in the Gulf of Maine by a small
 462 amount $\sim 1\%$. The western GOM shelf region weakly deamplified by 1-3% in the FS8 design, but
 463 this was not observed in the other L_x designs.

464 Although local differences in RE are illustrated in Figure 5, the CAFE curves demonstrate
 465 remarkable similarity in 99% of the comparison zone between the L_x and FSx solutions (i.e., above
 466 the thick 1% cumulative area line) for both the M_2 and K_1 elevation amplitudes (Figure 6). The
 467 CAFE curves for the M_2 are asymmetrical and indicate more of the domain has a positive error,
 468 which is accentuated in the tails below the 1% cumulative area line. While all the solutions in this
 469 experiment have achieved a converged solution, the FS6 and FS8 contain less positive RE than the
 470 L_x designs, while the opposite is true for the negative crossing although the difference is marginal
 471 (1-2%).

472 The relatively coarser L250 (+4.0% RE) and FS2 (+3.9% RE) mesh designs exhibited only
 473 slightly larger positive errors in the M_2 elevation amplitude as compared to L50 and the FS8 de-
 474 sign. These differences are marginal considering the 4 million total vertex count difference between
 475 the fine and coarse mesh designs (i.e., L50 and FS8 vs. L250). For the K_1 , all meshes have con-
 476 verged solutions to our tolerance and respond far less to alterations in mesh design than the M_2 .

480 3.2 Mesh size gradation

481 The concept of grading is a key capability of unstructured mesh finite element or finite vol-
 482 ume modeling in which coarse elements in the far-field grade smoothly into the more finely re-
 483 solved region of interests where fine resolution is necessary to capture the physical system and/or
 484 the hydrodynamic response to efficiently discretize regional and global ocean domains. This grada-
 485 tion rate between zones of variable resolution can greatly influence the number of vertices in the
 486 mesh (Figure 7). Elemental size grading has been based on solution gradients as well as bounding
 487 an estimate of the Courant number to encourage numerical stability [Luetlich and Westerink, 1995];
 488 however, the grade can also be based on geometric criteria by ensuring that neighboring mesh el-
 489 ement sizes cannot enlarge too quickly [Persson, 2006], i.e., the gradation is a bound on the max-
 490 imum relative increase in edgelenhth between adjacent elements. It is understood from a general
 491 modeling point of view that excessive gradation rates lead to triangles with skewed triangles con-
 492 taining acute or obtuse angles, which can impact the stability and numerical accuracy of the model

493 [Massey, 2015; Shewchuk, 2002]. Further, the analysis by Hagen *et al.* [2000] for one dimensional
 494 domains demonstrates that a high gradation value ($g \approx 0.5$) leads to the introduction of odd order
 495 truncation error term, which lowers the order of the method to first-order accurate and/or degrades
 496 the local/global accuracy.

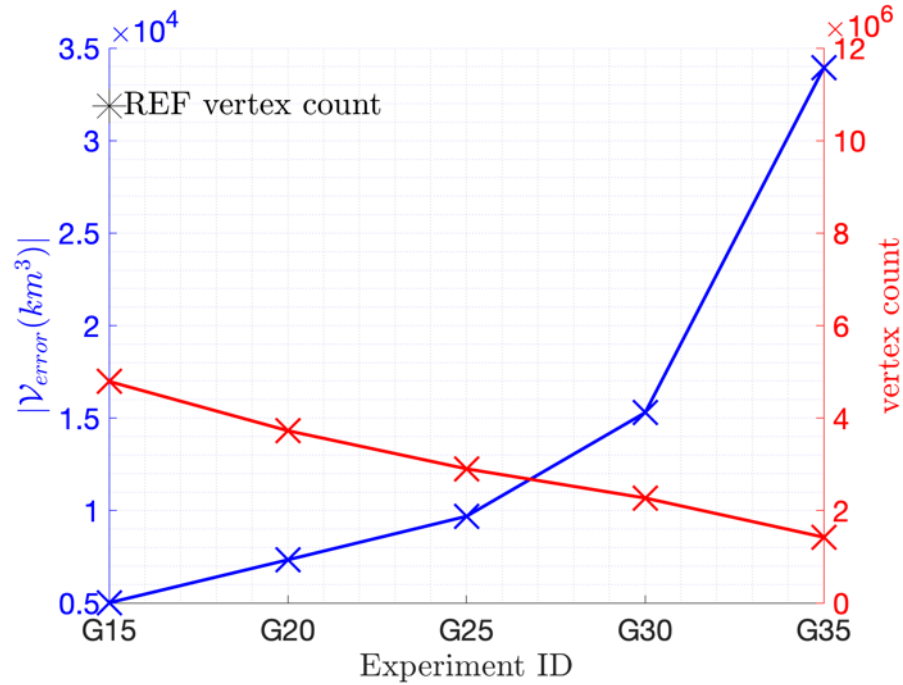
497 Fundamentally, the gradation rate will impact many aspects of the mesh design at once. A
 498 higher valued mesh size gradation will degrade the approximate representation of the seabed topog-
 499 raphy by creating comparatively coarser mesh sizes away from the targeted zones of fine res-
 500 olution. As was described in Table 1, the meshes that vary the gradation rate utilize a minimum
 501 resolution of 50-m along the shoreline (L50). Note that the mesh generator is bounding the gra-
 502 dation rate above by the user-defined parameter value only on the mesh size function and it is as-
 503 sumed that given the convergence of the mesh generator the gradation rate is similarly bounded in
 504 the triangulation (Section 2.4). Coarser mesh sizes tend to smooth the interpolation of seabed fea-
 505 tures onto the mesh vertices and this data interpolation effect can be quantified in the meshes by
 506 calculating the overall volume enclosed by the mesh while holding the shoreline boundary fixed
 507 (i.e., the surface area of the total mesh is constant). Thus, similar to the shoreline approximation
 508 error (Eq. 5), the seabed approximation error is calculated as the absolute difference in total vol-
 509 ume from the REF mesh:

$$\mathcal{V}_{error} = |V_{ID} - V_{REF}| \quad (6)$$

510 where V is the total mesh volume for the mesh denoted by ID and is calculated as the sum of all
 511 the mesh element volumes. An element volume is calculated by multiplying the average depth of
 512 the element by its area. Since the REF mesh employs uniform high resolution mesh sizes through-
 513 out the nearshore and continental shelf zones (c.f., Figure 1), it represents the seabed surface with
 514 the smallest approximation error. Note that the data interpolation approach we are using is a grid-
 515 scale average (Section 2.3) and is not a globally conservative interpolation scheme. From Figure 7,
 516 it is apparent that there is a diminishing reduction in the total vertex count of the mesh with in-
 517 creased gradation. For the purposes of this study, we were not able to explore meshes with gra-
 518 dation greater than 35% due in Experiment 3 (G_x) due to the introduction of triangles with very
 519 skewed aspect ratios and obtuse and acute angles that created numerical accuracy issues.

528 The increase in mesh size gradation from 15% to 35% leads to a highly amplified error pat-
 529 tern in the NA region for both M_2 and K_1 constituents as well as along the MAB for M_2 (Fig-
 530 ure 8). In the NA subdomain (Gulf of Maine), the M_2 RE is increased from 2-5% for G15 to 10-
 531 21% for G35 (colors are saturated in Figure 8a), in which the maximum RE is focused on the
 532 Georges Bank. In contrast to the response in the M_2 's RE, the K_1 's RE is nearly uniformly de-
 533 graded from -3% for G15 to -6% for G35 in the NA subdomain. The M_2 RE in the MAB, SAB,
 534 and eastern GOM tends to weakly deamplify by approximately 1% to 5% along the continental
 535 shelf zones. In contrast to the shoreline approximation experiment, a relatively large deamplifica-
 536 tion of the M_2 RE occurs in both the Chesapeake Bay and Delaware Bay as the gradation is en-
 537 larged to 35% (Figure 8a,b). The M_2 RE reaches as high as 15% in this region for the G35 experi-
 538 ment (colors are saturated in Figure 8a).

542 As the mesh size gradation grows, the tidal elevation amplitudes start to diverge substantially
 543 from the REF solution (Figure 9). In 99% of the comparison zone, the G15 mesh has an M_2 error
 544 between -1.3% and +3.0% RE whereas G35 has between -5.0% and +15% RE. Furthermore, the
 545 G35 mesh design exhibits between -5.5% and +6.5% K_1 RE in the 99% comparison zone, which
 546 is compared to -3.0% and +0% K_1 RE for G15. Unlike the shoreline experiment where all meshes
 547 converged (based on the $\pm 5\%$ threshold definition of convergence), only the G15 mesh converges
 548 for the M_2 constituent, and the G15 and G25 meshes converges for K_1 . However, it's important
 549 to note that the tendency of the solution is convergent as the RE reduces when the mesh sizes are
 550 made finer with lower gradation bounds.

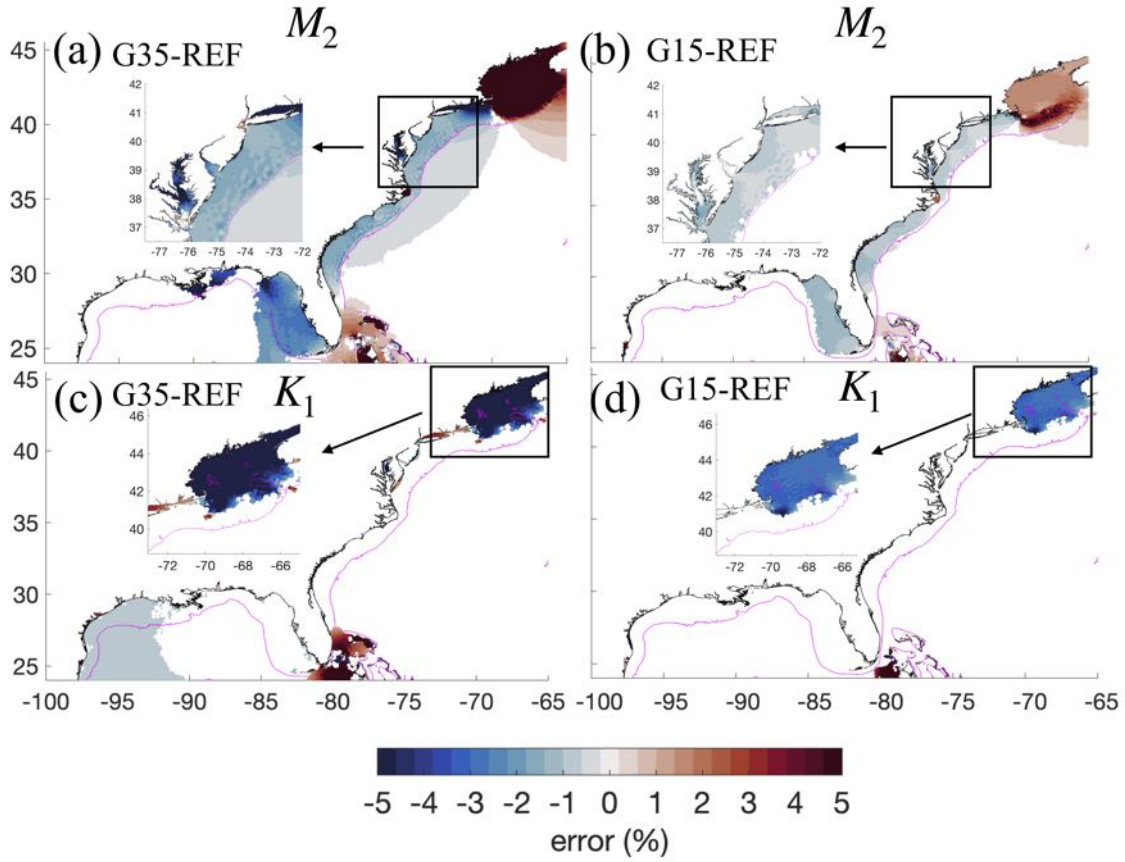


520 **Figure 7.** The seabed approximation error V_{error} (Equation 6) on the left-axis (blue x's) as the mesh size gradation
 521 is increased from 15% to 35% in increments of 5% while the shoreline boundary is held fixed (i.e., area of domain
 522 is constant). The total vertex count in each mesh on the right axis (dashed red x's). The REF mesh vertex count is
 523 demarcated by a black asterisk in the top left corner of the figure.

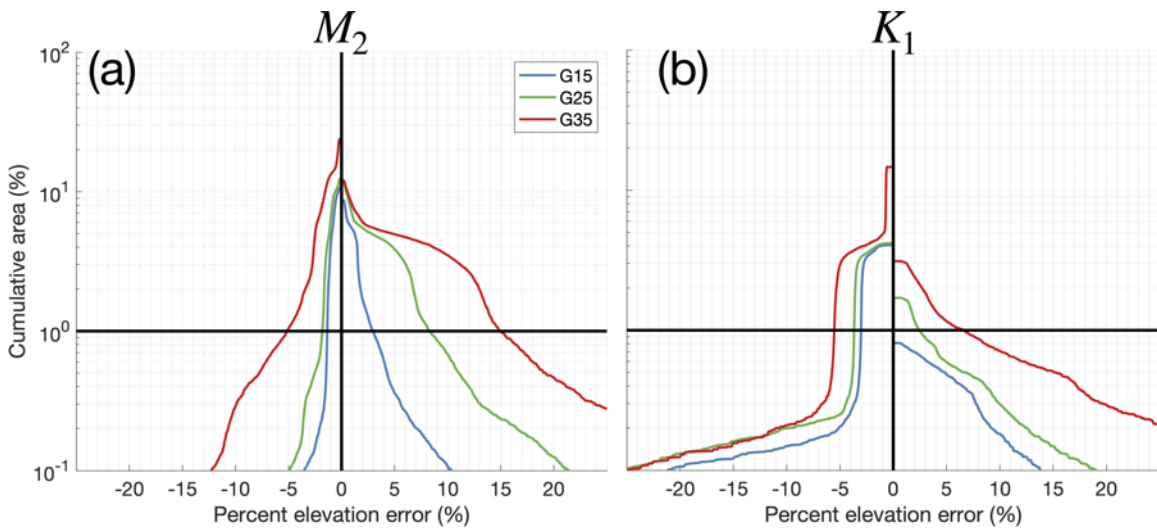
551 3.3 Resolution along bathymetric gradients

552 The main motivation for increasing the horizontal resolution in the open ocean is to more ac-
 553 curately represent sharp seabed gradients, particularly those that characterize the continental shelf
 554 break and slope. The representation of these seabed gradients is captured with the topographic-
 555 length-scale S_x (Figure 2 and Table 1). The topographic-length-scale S_x is considered a useful
 556 mesh heuristic [see *Greenberg et al.*, 2007, for a review] to aid in the modeling of shelf break dy-
 557 namics [*Huthnance*, 1995; *Hannah and Wright*, 1995; *Luettich and Westerink*, 1995], subtidal dy-
 558 namics [*Loder*, 1980; *Chen et al.*, 2016], and internal tide generation processes [*Xing and Davies*,
 559 1998] and their effects on barotropic tides [*Pringle et al.*, 2018a,b]. Further, *Hagen et al.* [2001] has
 560 demonstrated that an inadequate prescription of resolution along sharp seabed gradients is a source
 561 of numerical truncation error for tidal models. However, as $b \rightarrow 0$, the S_x meshing criteria fails
 562 for some areas as resolution becomes excessively fine in shallow depths and creates element sizes
 563 which can lead to numerical instabilities.

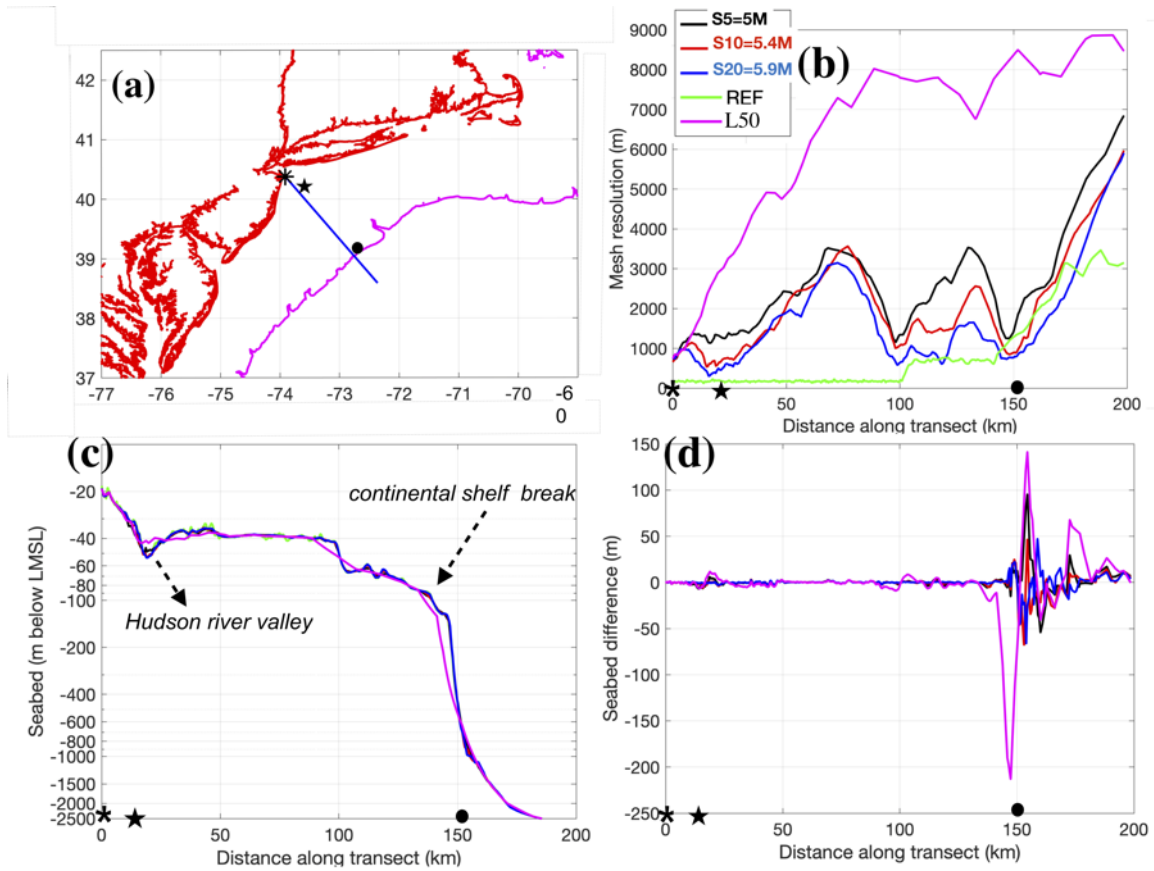
564 The topographic-length-scale S_x parameter must consider the trade-off between the improve-
 565 ment to the solution of barotropic tides and the additional mesh vertex count. *Chen et al.* [2016]
 566 suggested resolution sizes between 3.3 to 6 km to capture the shelf break and 2 km to capture
 567 the deep slope in the Arctic Ocean. *Lyard et al.* [2006] suggested S15 globally using quadratic fi-
 568 nite elements, but noted that this value was restricted in its spatial application due to the excessive
 569 computational expense it incurred. In our studies, besides the excessive computational expense in-
 570 curred by the additional degrees-of-freedom, we have found that using S_x larger than S20 leads to
 571 resolution along the shelf-break that can extensively restrict the feasible time step (i.e., time step of
 572 2 s with Courant number bounded to 0.5). Note that the S_x heuristic is only applied where $b > 50$
 573 m to avoid issues in shallow depths, where many small-scale features such as channels that we
 574 propose an alternative strategy to resolve documented later on.



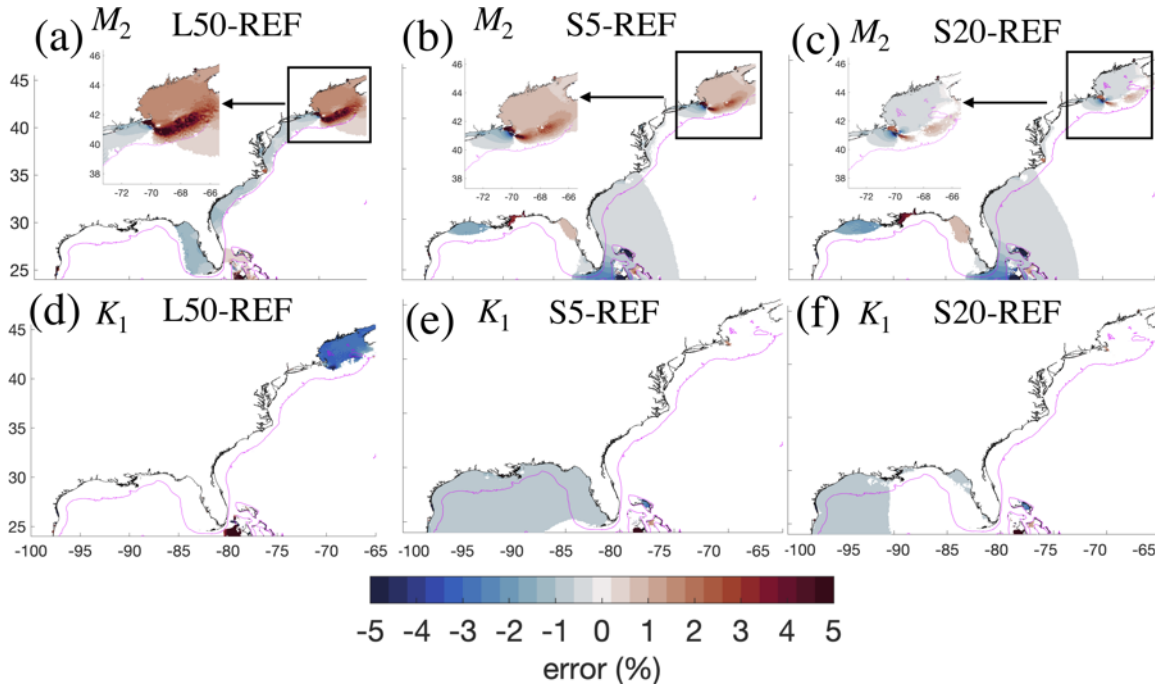
524 **Figure 8.** Panels (a)-(b) illustrate the RE in the M_2 elevation amplitude from the REF solution as the mesh gradation
 525 bound is increased to 35% while in panel (b) it is kept low at 15%. Panels (c) and (d) are the same as panels (a)-(b)
 526 but for the K_1 elevation amplitude. The 250-m isobath contour is drawn as a magenta line in each panel for reference.
 527 Insets are shown to reflect areas that are described in the text.



539 **Figure 9.** The cumulative area fraction error (CAFE) in the comparison zone (c.f., Figure 1) in panel (a) for the M_2
 540 elevation amplitude and panel (b) for the K_1 harmonic elevation amplitude using the meshes created for the mesh size
 541 gradation experiment.



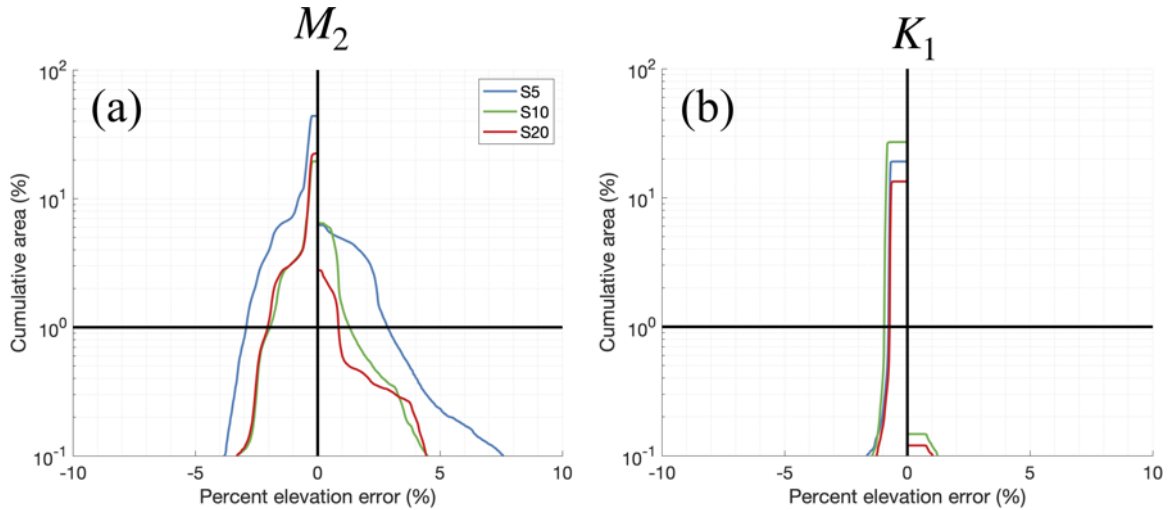
575 **Figure 10.** (a) A cross-shelf transect in the MAB region indicated in blue with the asterisk indicating the start of
 576 the transect, the magenta line is the 250-m isobath, and the red line is the shoreline; (b) the mesh resolution along the
 577 transect for the S_x , REF, and L50 meshes. Panel (c) illustrates the seabed topography along the transect for each mesh.
 578 Panel (d) illustrates the difference in seabed topography from each mesh and the REF mesh along the transect.



591 **Figure 11.** Panels (a)-(b) depict the M_2 elevation amplitude RE for solutions computed on the S_x meshes. Panels
 592 (c)-(d) depict the RE the K_1 elevation amplitude.

579 In Experiment 4 (S_x) the vertex count is increased by 4% to 20% over the L50 mesh, accom-
 580 panied by an improvement to the approximation of seabed profile, as illustrated along a transect
 581 spanning the cross-shelf direction in the MAB region (Figure 10). Mesh resolution in the vicini-
 582 tity of the shelf break zones is enhanced to approximately 1.2 km and 0.8 km for S5 and S20, re-
 583 spectively. A point worth noting is that seabed features exist on the continental shelf break, such
 584 as the drowned Hudson river valley, which will otherwise be completely smoothed over without
 585 the S_x heuristic. In comparison, without S_x , resolution is coarser than 8 km (close to the maxi-
 586 mum resolution size) in the vicinity of the shelf break (see L50 in Figure 10b), which tends to
 587 shift the break zone shoreward and result in a smoother and more gradual representation of the
 588 seabed profile along the transect (Figure 10c). The S_x heuristic results in a clear improvement in
 589 the depiction of the seabed profile. S20 had seabed profile differences of less than 50 m from the
 590 REF mesh, whereas the seabed profile difference for L50 is as large as 200 m (Figure 10d).

593 The finer resolution along seabed gradients using S_x leads to a significant overall reduction
 594 in the RE pattern associated with the M_2 elevation amplitude in the MAB and NA subdomains
 595 (Figure 11a-c), with the M_2 error pattern diminished almost entirely for S20 (Figure 11c). Note
 596 that although the largest RE is co-located with the phase convergence zone of the M_2 tidal species
 597 in the MAB and NA domain (where the elevation amplitude is zero), the RE is not confined to
 598 solely the amphidromic point and emanates around the entirety of the NA subdomain. Similarly,
 599 for the K_1 elevation amplitude, an approximately -4% RE in the NA subdomain for the L50 (i.e.,
 600 S0) mesh is undetectable for any of the S_x meshes (Figure 11d-f). Contrastingly, in the GOM do-
 601 main the application of S_x tends to introduce differences from the REF mesh rather than reduce
 602 them. Upon inspection, the REF is less resolved in parts of the GOM, Bahama Banks, and the
 603 Caribbean Sea (c.f., Figure 1) in comparison to the S_x meshes here, possibly explaining this re-
 604 sult. The S20 mesh in particular contains finer resolution than the REF mesh along the shelf break
 605 zones of the western GOM, which is co-located with a persistent albeit weak negative RE in the
 606 M_2 in the S10 and S20 solutions.



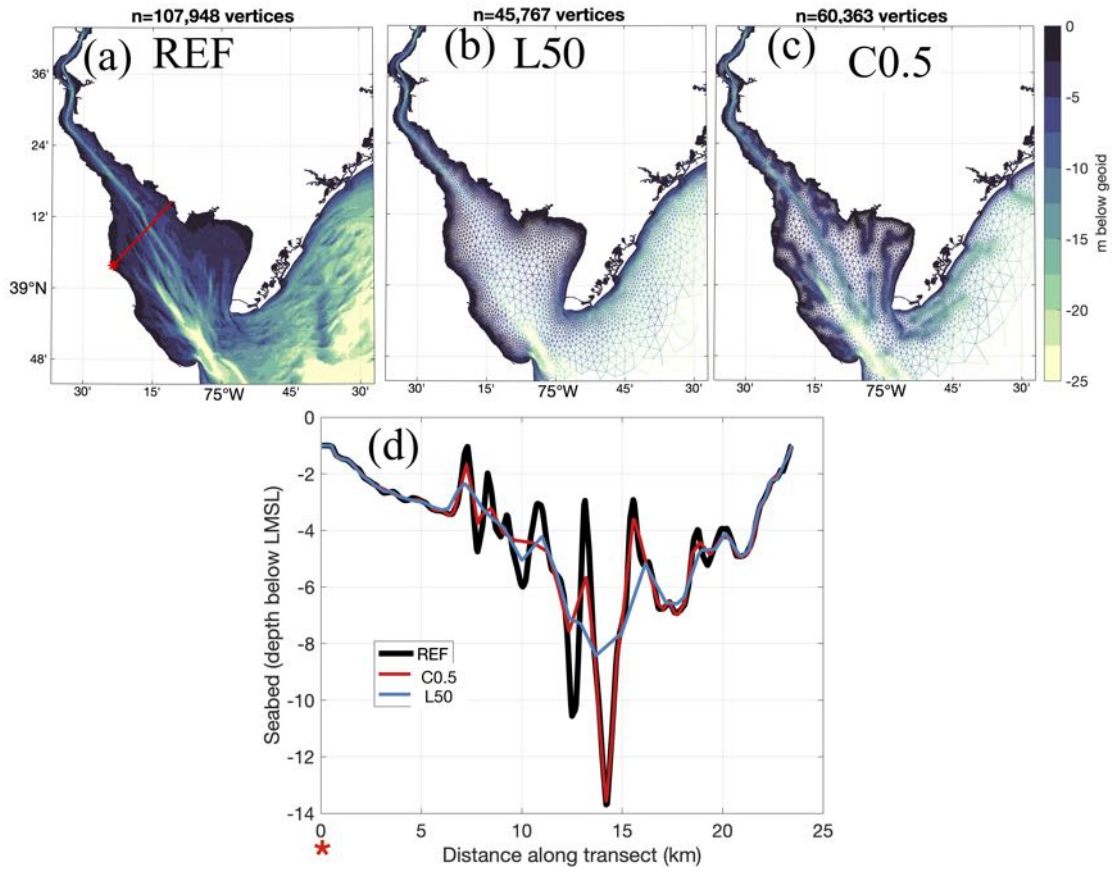
607 **Figure 12.** The cumulative area fraction error (CAFE) curves in the comparison zone for the S_x meshes.

608 The CAFE curves for M_2 and K_1 (Figure 12) clearly illustrate that increased resolution along
 609 seabed gradients leads to a converged solution in 99% of the domain for S5, S10 and S20 accord-
 610 ing to our definition of convergence ($\pm 5\%$). The S5 mesh has the largest M_2 error of $\pm 2.9\%$ RE in
 611 99% of the comparison zone, which predominantly corresponds to the errors in the MAB and NA
 612 domains. As evident from Figure 12, the K_1 was less sensitive to the choice of S_x mesh design
 613 than M_2 , with differences of approximately $\pm 3\%$ in 99% of the comparison zone. However, the S_x
 614 for the K_1 consistently and substantially (by 10 to 15%) reduced the spread of the tails in 0.1% of
 615 the domain. As was illustrated in Figure 12(d),(e),(f), the negative underprediction for the K_1 in
 616 the NA and MAB domains were consistently reduced with the application of the S_x heuristic.

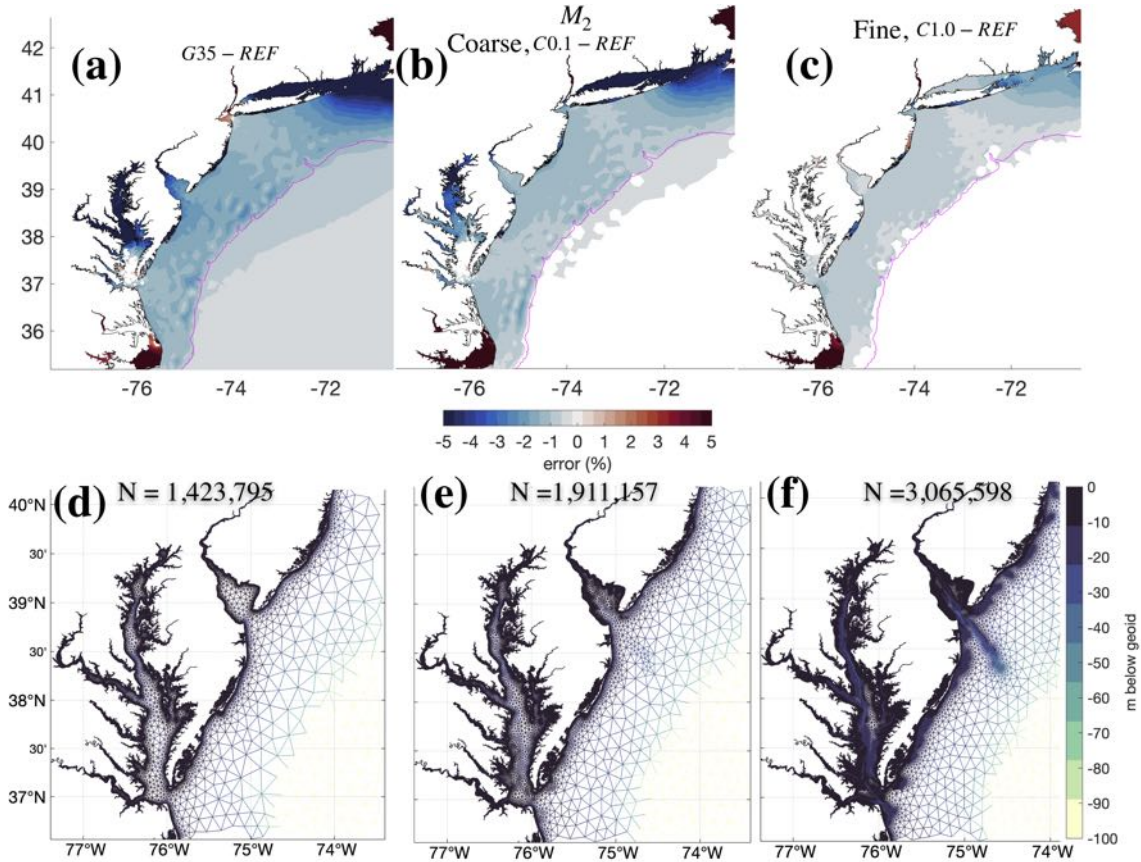
617 3.4 Cross-sectional representation of estuarine channels

618 Estuarine hydrodynamics are controlled by the depth and form, together referred to as the
 619 morphology of the estuarine seabed [Dronkers, 1986; Parker, 1991; Friedrichs, 2010; Prandle,
 620 2003]. Thus, when designing a model to simulate coastal hydrodynamics, it is important to ap-
 621 ply sufficient resolution to approximate the nearshore seabed topography. In particular, coarse mesh
 622 resolution in the presence of fine and narrow channelized bed forms will alias the channel's cross-
 623 sectional profile (Figure 13) and lead to the inaccurate computation of transports, fluxes, and fric-
 624 tional resistance [Molines *et al.*, 1989; Greenberg *et al.*, 2007]. In the broader context of mesh
 625 generation techniques for coastal ocean modeling, mesh design heuristics that target resolution in-
 626 versely proportional to seabed's depth [e.g., Westerink *et al.*, 2008] will also tend to coarsen the
 627 resolution in the center of the estuary in the deepest component of the tidal channel. Thus, exist-
 628 ing techniques used to build models do not adequately resolve long and narrow channelized bed
 629 forms that are critical to conveying water into and throughout inland water systems.

630 An automatic mesh size function C_x that localizes finer mesh resolution in close proximity
 631 to the thalwegs of important estuarine channel morphology was developed as part of the *Ocean-
 632 Mesh2D* meshing software suite [Roberts *et al.*, 2018]. An example of a mesh created with the
 633 *estuarine channel* mesh size function C_x is illustrated in Figure 13(c) for the Delaware Bay estu-
 634 ary located in the MAB region. With 44% less vertices than REF in this subset of the ECGC, the
 635 C0.5 mesh represents the cross-sectional area of the deepest thalweg in the estuary with the same
 636 accuracy. In comparison, the L50 mesh is only 8 m deep at the thalweg compared to almost 14 m
 637 in the REF and C0.5 meshes. Notice that other less pronounced thalwegs are not captured by C0.5
 638 due to the application of coarser resolution.



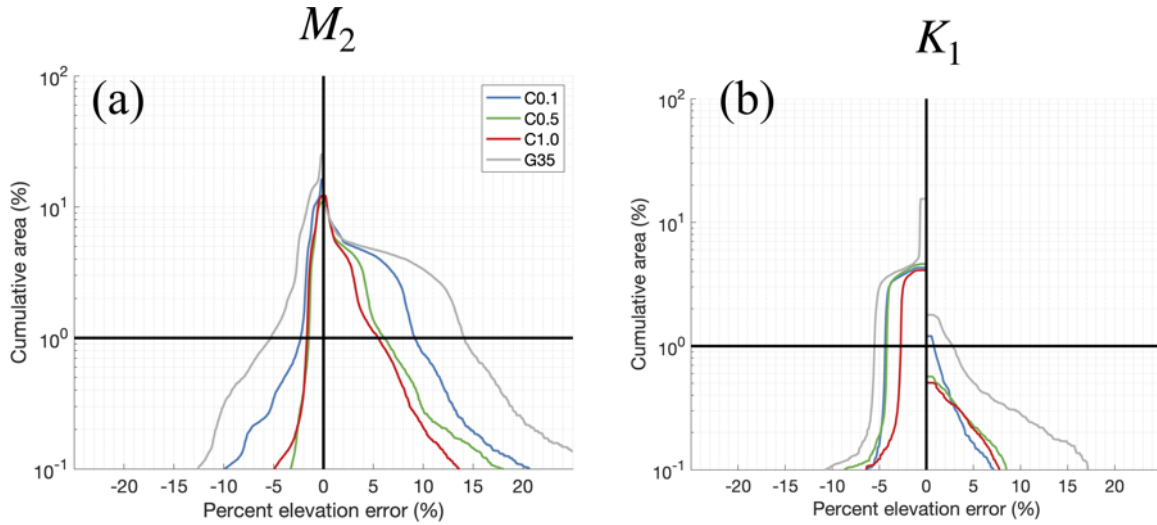
630 **Figure 13.** Panels (a)-(c) show sections of meshes in the Delaware Bay estuary and their interpolated seabed data to
 631 demonstrate the effect of variably resolving channelized seabeds. Panel (d) illustrates the cross-sectional profile of a
 632 tidal channel that is annotated as a red line in panel (a).



651 **Figure 14.** Panels (a)-(c) illustrate the error in the M_2 elevation amplitudes for solutions computed on meshes that
 652 variably resolve drainage networks that approximate tidal channels. Panels (d)-(f) indicate the mesh and interpolated
 653 seabed topography onto the mesh vertices. On panels (d)-(f), the total vertex count is annotated. Note the vertex count
 654 indicated in panels (d)-(f) represents the total vertex count in the mesh.

642 The effects of the *estuarine channel* mesh size function have been investigated in Experi-
 643 ment 5 (C_x) using a mesh size gradation of 35% (G35). A higher mesh size gradation motivates
 644 the resolution targeting approach because mesh element sizes are relaxed quickly away from the
 645 channel thalwegs where finer resolution is applied, thus obtaining a mesh with overall fewer ver-
 646 tices than without the targeting approach. Furthermore, a lower mesh size gradation (e.g., 15%)
 647 would lead to finer resolution in the center of the estuary where the thalweg may be located and
 648 may already adequately resolve the channels cross-sectional profile. The mesh vertex count in the
 649 finest C_x mesh (C1.0) is increased by more than two-fold from the G35 mesh to approximately 3.1
 650 million vertices (Figure 14d-f), still approximately 60% of the G15 mesh vertex count.

655 The refinement of the estuarine channel network primarily impacts the M_2 elevation ampli-
 656 tude solution locally in the estuarine regions of the MAB and NA subdomains (Figure 14a-c). A
 657 consistent reduction in M_2 RE from the high mesh size gradation solution (G35) is observed lo-
 658 cally, particularly the 5-10% RE under-prediction error in large estuaries such as the Chesapeake
 659 Bay, Delaware Bay, and Long Island Sound. The remaining under-prediction error in these large
 660 estuaries is under 1-2% RE for the C1.0 mesh. Some smaller-scale estuarine systems also exhibit
 661 reduction to the RE. For example, the large negative error for G35 (<-5% RE) in Barnegat Bay
 662 (c.f., Figure 1) in the MAB region is reduced to the point that the error changes sign for C1.0 (+1-
 663 2% RE) (Figure 14a-c).



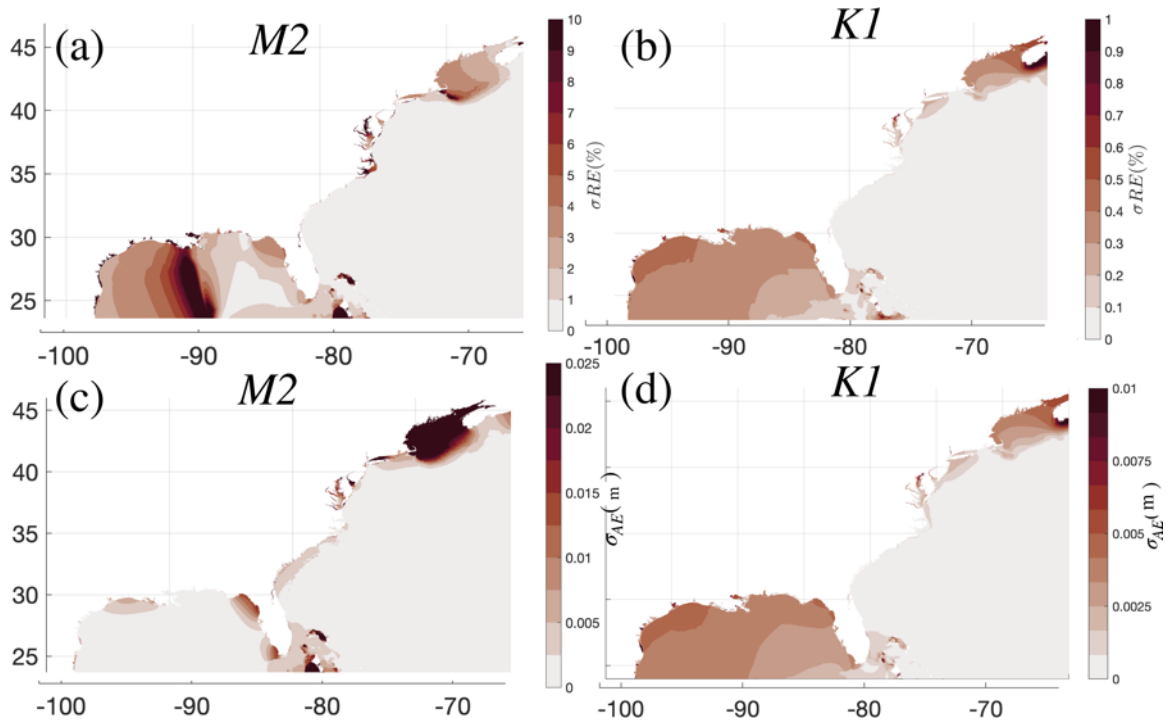
664 **Figure 15.** The cumulative area fraction error (CAFE) curves in the comparison zone for the Cx meshes.

665 Similarly, the CAFE curves also demonstrate a consistent reduction in M_2 and K_1 RE in the
 666 comparison zone for the Cx meshes and a substantial reduction of RE as compared to the solution
 667 computed on G35 (Figure 15). While none of the meshes have converged with the application of
 668 resolution along estuarine channels, the sequence exhibits convergence. Despite the approximately
 669 0.7 million vertex count difference between the C0.5 (2.4 million vertices in total) and C1.0 (3.1
 670 million vertices in total) meshes, their associated solutions perform similarly suggesting diminish-
 671 ing performance gains with finer resolution along estuarine channels. In 99% of the comparison
 672 zone, the C1.0 mesh M_2 error ranges between -1.6% and +5.5% RE, and -2.8% to +0% RE for the
 673 K_1 producing non-converged solutions for the M_2 but converged solutions for the K_1 . Nevertheless,
 674 the narrowing of the error range in 99% of the comparison zone for the Cx meshes over that of the
 675 G35 mesh (-5.0% to +15% for M_2) even though the same 35% gradation is employed is substan-
 676 tial.

677 3.5 Summary of experiments

678 3.5.1 Predominant variability

679 A summary of the variation in amplitude errors throughout the ECGC region in response
 680 to changes in mesh resolution from all 15 meshes over the five experiments (Table 1) is summa-
 681 rized by taking the standard deviation (σ) of RE and the dimensional error, $AE = A_{ID} - A_{REF}$
 682 (Figure 16). The greatest changes in the M_2 elevation amplitudes are collocated with M_2 phase
 683 convergence zones and amphidromic points (c.f., Figure 1), and in some large and small estuaries
 684 such as the Chesapeake Bay and the Delaware Bay. In the Gulf of Maine, NA which is a resonant
 685 basin with a large tidal range (2-10 m), σ_{RE} is 1-4% and σ_{AE} is well above 2.5 cm for M_2 . The
 686 K_1 differences in the Gulf of Maine are also larger than most other regions. In the GOM which
 687 has a small semidiurnal tidal range, σ_{RE} is large in the central region around the convergence zone
 688 for M_2 but this only corresponds to less than around 2 mm of dimensional variability (σ_{AE} is very
 689 small). In general, the K_1 is noticeably less responsive to changes in mesh resolution with σ_{RE}
 690 barely exceeding 1%. The K_1 exhibits the greatest variation in the NA subdomain (Gulf of Maine),
 691 in large estuaries, and throughout most of the GOM. The relatively small response in the K_1 is to
 692 be expected given that it is less energetic and has a longer wavelength than the M_2 , and it does not
 693 typically exhibit resonance on wide shelves [Clarke and Battisti, 1981].



694 **Figure 16.** Standard deviation of the relative error (σ_{RE}) in (a) the M_2 and (b) the K_1 elevation amplitudes for all
 695 15 meshes from the five experiments (Table 1). Panels (c) and (d) are the same but for the standard deviation of the
 696 dimensional errors (σ_{AE}). Note the differences smaller than the significance threshold defined in this paper *are* shown
 697 and that the colorbars are *not* the same between panels (a) and (b).

3.5.2 Numerical error versus physical approximation error

An outstanding issue with the results is that the numerical and physical approximation component of error are intertwined both contributing to the RE observed in the experiments. As the approximation of the bathymetry and shoreline boundary becomes more accurate with the application of finer resolution, the study of convergence in the tidal response becomes challenging as new bathymetric and shoreline features emerge. From a model design point of view, the isolation of the numerical component of the tidal error can provide clarity into how to improve the physical approximation component of error.

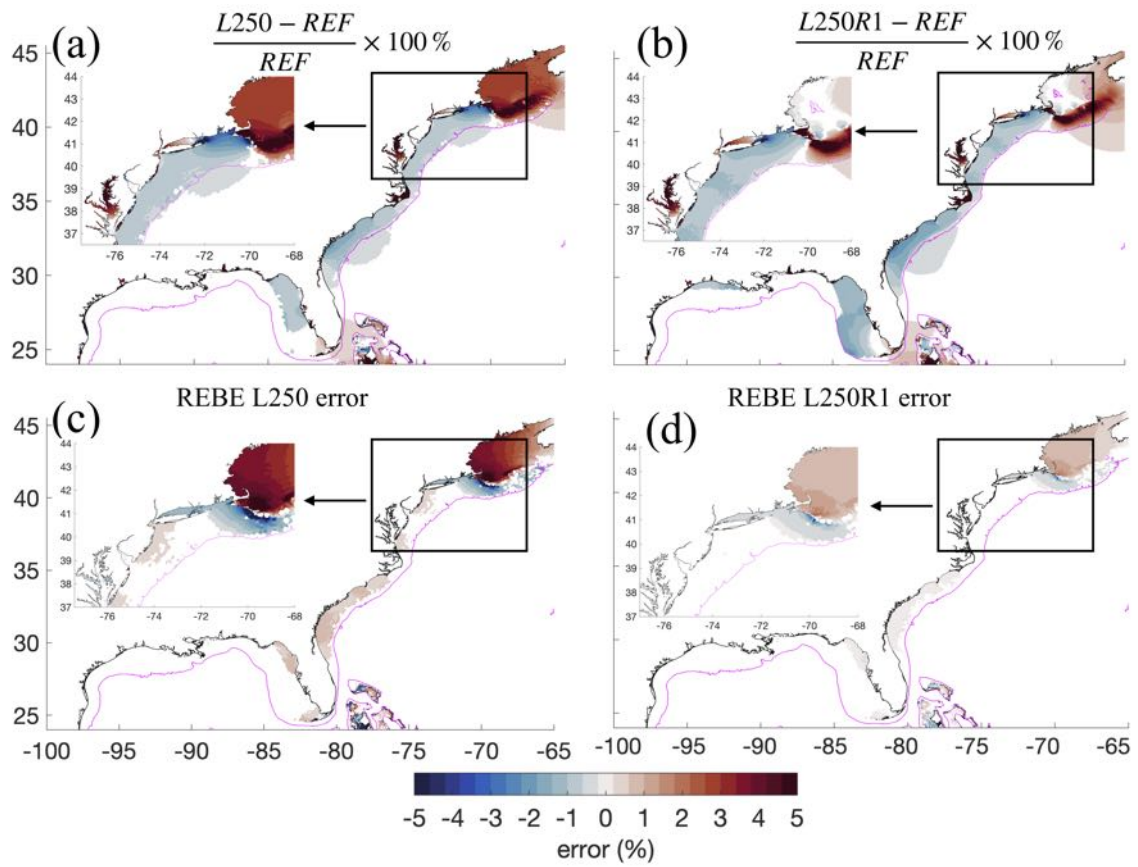
To isolate the numerical error in the tidal harmonics studied here, changes in the physical domain approximation was held constant by refining the relatively lightweight L250 mesh so that all triangular edges, except for those within 1° of the open ocean boundary, were bisected about their midpoints producing four new triangles for every pre-existing one following a shape-preserving scheme [Engwirda, 2014]. The bathymetry from the L250 mesh was linearly interpolated onto this new refined mesh (L250R1) ensuring that the approximation of the seabed topography are identical between the two meshes. Further, the bisection of the elements preserves the representation of the shoreline geometrical features between meshes. The numerical error was then estimated with Richardson extrapolation [Roache, 1994; Blain et al., 1998]. In order to use this approach to estimate numerical truncation error, it was first verified that the leading order error terms indeed controlled the numerical convergence (i.e., asymptotic regime), spatial errors were found to be much greater than the time discretization errors, and the ADCIRC solver in the current configuration was a second order accurate method in space and time [Luettich and Westerink, 2004]. The order of convergence was verified to be 2nd order accurate by refining L250R1 once more producing L250R2.

The Richardson extrapolation base error (REBE) following [Roache, 1994] is calculated to estimate numerical error with the following formulas:

$$\begin{aligned}
 REBE[\text{coarse mesh}] &= \frac{\epsilon r^n}{(r^n - 1)} \\
 REBE[\text{fine mesh}] &= \frac{\epsilon}{(r^n - 1)} \\
 n &= \text{spatial order of ADCIRC} = 2 \\
 \epsilon &= 100 \times \frac{\tilde{f}_{L250R1} - \tilde{f}_{L250}}{\tilde{f}_{REF}} [\%] \\
 r &= \frac{X_{L250}}{X_{L250R1}} = 2 = \text{refinement factor}
 \end{aligned} \tag{7}$$

where \tilde{f}_{L250} and \tilde{f}_{L250R1} are the solutions computed on the original and refined meshes and \tilde{f}_{REF} is the solution computed on the reference mesh. X_{L250} and X_{L250R1} denote the spatially varying mesh sizes throughout the computational domain.

The REBE (herein the numerical error) for the L250 and L250R1 M_2 amplitude elevation is presented in Figure 17c,d and compared against the total error that was calculated from the REF solution using Equation 1 (i.e., RE) like was performed in the rest of the paper (Figure 17a,b). There is a similarity in the numerical and total error estimates particularly in the NA subdomain where the magnitude of both errors are 3-5% for the L250 mesh and diminish to 1-2% for the L250R1 mesh. However, the estimate of the greatest magnitude numerical error is co-located with the periphery of the Georges Bank near sharp seabed topographic gradients, while the total error is spread across the entire Georges Bank. In general, a weaker reduction in the total error is observed compared to the numerical error. In particular, the total error is not reduced over the Georges Bank or along most of the SAB and MAB coastline (Figure 17a-b). However, the numerical error is reduced almost everywhere to below the significance threshold. For instance, the refinement of L250 to L250R1 reduces the numerical error estimate in the Chesapeake Bay estuary in the MAB re-



726

Figure 17. An estimate of the numerical error calculated via Richardson extrapolation following [Roache, 1994] obtained by refining the L250 mesh using a four-to-one refinement strategy to preserve the approximate problem.

727

740 gion markedly. However, the total error does not diminish in the MAB region (particularly the
 741 Chesapeake Bay), which suggests these regions are more responsive to changes in the physical do-
 742 main approximation (Figure 17). Overall, even though the numerical error has become insignificant
 743 (1-2% in magnitude) and converged as the mesh has been refined, relatively large shoreline and
 744 seabed domain approximation errors still remain in the Chesapeake Bay, the Long Island sound,
 745 and the Georges Bank ($\approx 1-5\%$). Thus, a method that will reduce the numerical error through an
 746 iterative refinement strategy, like LTEA, may still be incapable of improving the accuracy of the
 747 solution as compared to observations even if it minimizes the numerical truncation error as it can-
 748 not readily incorporate solution responses from un-resolved shoreline geometry scales.

749 3.5.3 Mesh design combinations

750 The previously described mesh size functions (Table 1) can be used in combination by taking
 751 the minimum of each individual function for each point in a regional or global domain [Conroy
 752 *et al.*, 2012; Roberts *et al.*, 2018]. Certain combinations of mesh size functions can be regarded as
 753 more or less efficient at sufficiently approximating the physical domain. For instance, if the user
 754 were to rely on a low mesh size gradation (e.g., 10-15%), the *estuarine channel* mesh size function
 755 becomes far less necessary because elements in proximity to the channel are already close to the
 756 resolution at the shoreline.

757 Based on our resolution targeting approach, a sequence of mesh designs with different com-
 758 binations of mesh size functions, all with a high gradation (35%), were built with the goal of main-
 759 taining the accuracy of tidal solution while significantly reducing the vertex count as compared to
 760 the REF mesh:

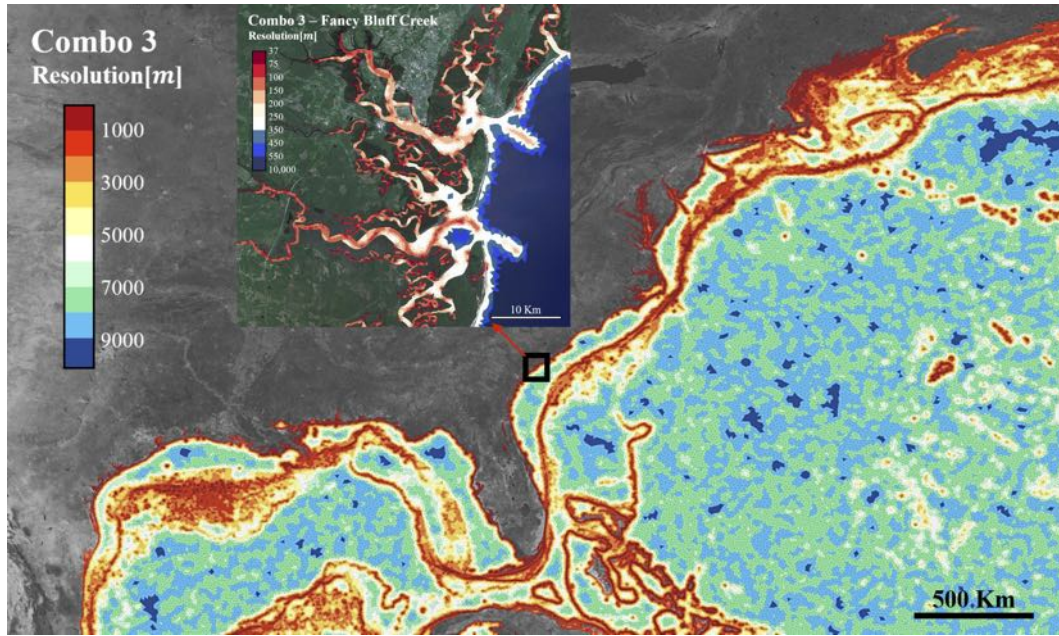
761 COMBO1: $\min(L50, S20)$ with $g \leq 35\%$ \rightarrow employs 50-m resolution everywhere along the shoreline
 762 (L50), a steep mesh size gradation of 35% (G35), and enhanced resolution on seabed gradi-
 763 ents (S20). A total of 2.3 million vertices.

764 COMBO2: $\min(FS2, S20)$ with $g \leq 35\%$ \rightarrow uses *feature size* function to vary mesh resolution between
 765 50 m and 250 m along the shoreline while maintaining a minimum of two elements across
 766 the width of the shoreline (FS2), a steep mesh size gradation of 35% (G35), and enhanced
 767 resolution on seabed gradients (S20). A total of 1.1 million vertices.

768 COMBO3: $\min(L50, S20, C0.5)$ with $g \leq 35\%$ \rightarrow uses *feature size* function to vary mesh resolution
 769 between 50 m and 250 m along the shoreline while maintaining a minimum of two ele-
 770 ments across the width of the shoreline (FS2), a steep mesh size gradation of 35% (G35),
 771 enhanced resolution on seabed gradients (S20), and enhanced resolution along estuarine
 772 channel features. A total of 1.3 million vertices.

773 The idea behind this sequence of mesh combinations (COMBO x) is to proceed from a more
 774 simple design and move towards a more complex design to test the additive effects, i.e., start with
 775 uniform shoreline resolution (COMBO1); use variable shoreline resolution (COMBO2); add addi-
 776 tional resolution along estuarine channels (COMBO3). COMBO1 begins with a high gradation rate
 777 and a large slope function parameter because of the resolution targeting that we think, and which
 778 the experimental results support, lead to more efficient designs. Figure 18 highlighting this target-
 779 ing approach by illustrating the resolution distribution for the COMBO3 mesh.

782 Similar to the error reduction patterns in Experiment 4 using fine resolution (500-1km) along
 783 sharp seabed gradients and a 15% gradation (c.f., Figure 11), the RE in M_2 for all COMBO x meshes
 784 is reduced significantly from the G35 mesh, primarily in the NA and MAB subdomains (Figure 19a-
 785 c). In fact, the S20's CAFE curve is largely similar to the COMBO x meshes. Thus, using S20 to
 786 resolve high gradient seabed topographic slopes effectively allows for a much higher elemental size
 787 expansion rate to conserve computational resources. Conspicuous positive values of RE near the
 788 Georges Bank in proximity to the M_2 's amphidromic point persists, but this is reduced from 10-
 789 21% for the G35 mesh to under 5% for all COMBO x meshes. The improvement to M_2 RE for the
 790 COMBO x meshes is also reflected in their CAFE curves (Figure 19d), which perform similarly to
 791 the S20 mesh in 99% of the comparison zone for the negative crossing (-1% to -2% RE), but con-



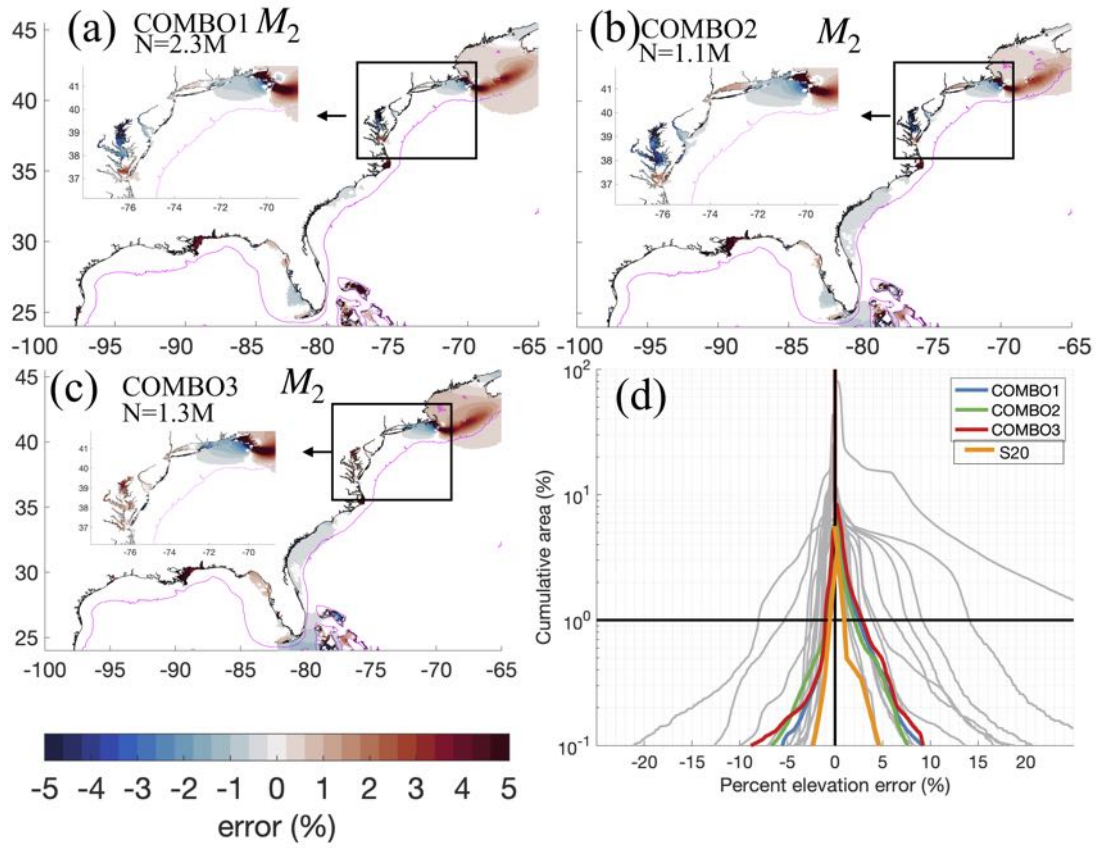
780 **Figure 18.** Elemental resolution distribution in the COMBO3 mesh, highlighting how fine resolution is targeted in
 781 narrow geometries and along seabed gradients and estuarine channels (see inset in Fancy Bluff Creek).

792 tain slightly larger RE for the positive crossing (+3% to +4% RE). Overall, the RE is substantially
 793 reduced from the +16% RE positive crossing for the G35 mesh.

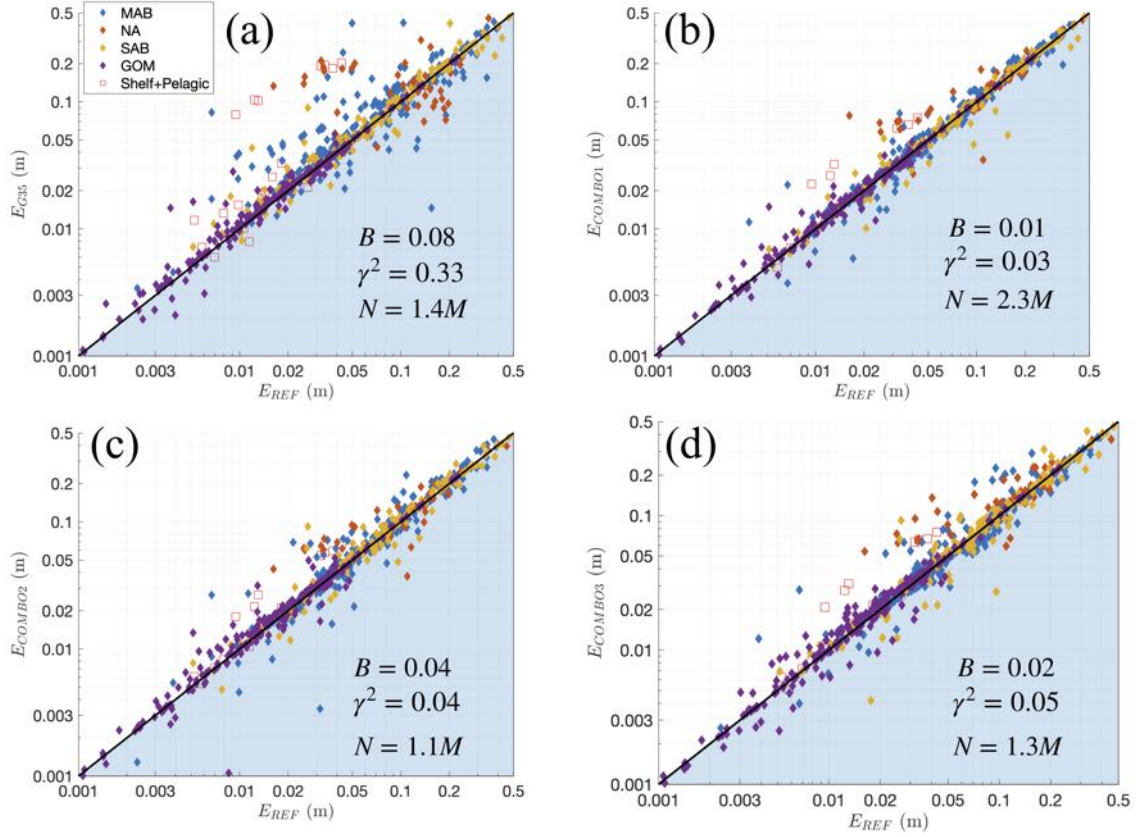
794 Furthermore, the resulting pattern of errors against measured harmonic data (Figure 20) for
 795 the COMBO x meshes approaches that of the REF mesh ($B = 0.01$ to 0.04 , $\gamma^2 = 0.03$ to 0.05). In
 796 comparison, the positive bias and spread of the errors is significantly greater for the G35 mesh (B
 797 $= 0.08$, $\gamma^2 = 0.33$) demonstrating substantial improvement in the tidal validation of the mesh with
 798 the application of the combinational designs.

807 The effect on M_2 RE when moving from a uniform shoreline resolution (COMBO1) to vari-
 808 able shoreline resolution (COMBO2) based on the feature size approach in the combination meshes
 809 is small (Figure 19a-b). Differences less than 1% are noticeable in the Long Island Sound, Delaware
 810 estuary, and around the Georges Bank and Gulf of Maine. Furthermore, the resulting pattern of er-
 811 rors against observations from REF is similar between COMBO1 and COMBO2, although the bias
 812 has increased to from 0.01 to 0.04 (Figure 20b-c). Considering that the usage of the FS x shoreline
 813 resolution in COMBO2 leads to 53% fewer vertices than in COMBO1, a small increase to the bias
 814 and variance is expected.

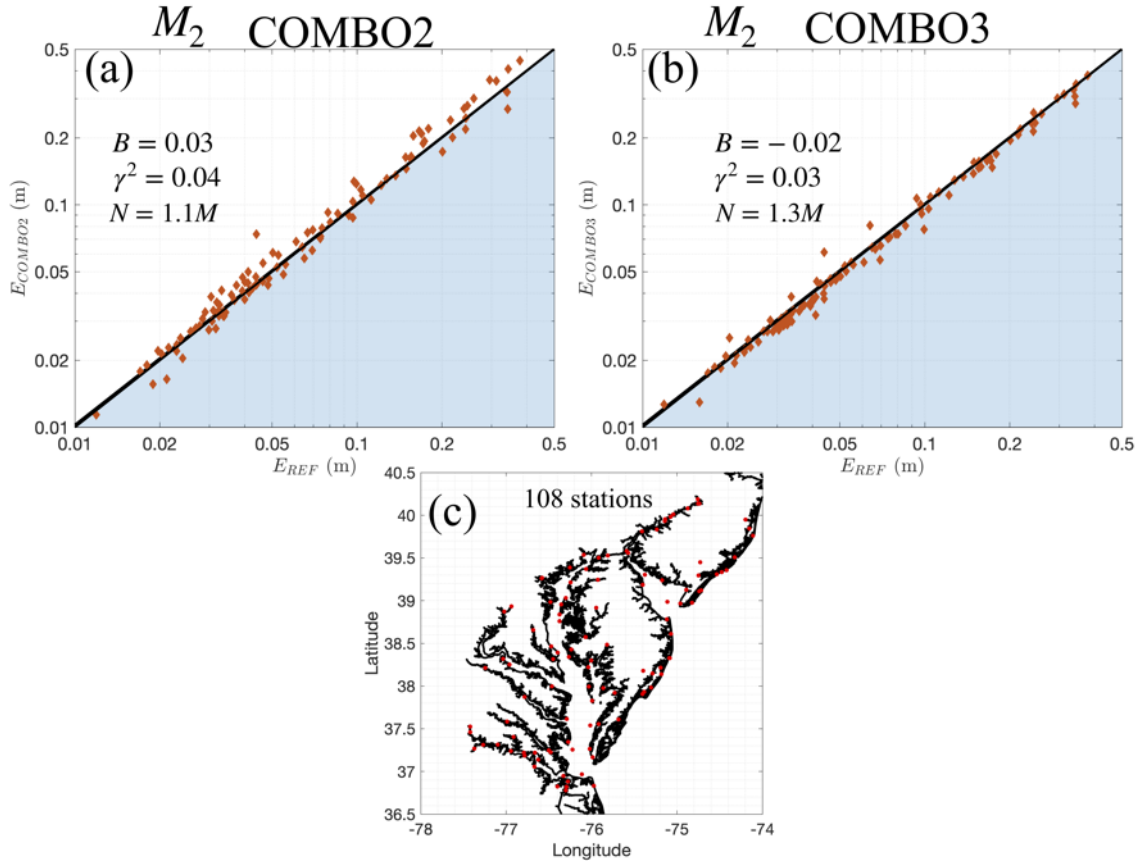
815 The effect on M_2 RE when additional resolution is placed along important estuarine chan-
 816 nels (COMBO3 versus COMBO2) can be important in localized regions. The overall picture, as
 817 illustrated through the CAFE curves (Figure 19d) and the domain-wide tide gauge error pattern
 818 (Figure 20), is relatively unaffected, as evidence by the relatively small change in measured statis-
 819 tics. Predominately, the region of positive RE over the Georges Bank and the Gulf of Maine is in-
 820 creased by approximately 1% when moving to the COMBO2 and COMBO3 meshes. However, RE
 821 is noticeably reduced in the Delaware Bay, Chesapeake Bay, and Long Island Sound to under +1%
 822 RE in most areas (Figure 19b-c). Focusing only on the tide gauges ($n = 108$) contained inside
 823 the MAB estuaries (Figure. 21), the effect of targeting finer resolution along the channels is fur-
 824 ther highlighted. The normalized bias is reduced from a positive bias in COMBO2 ($B = 0.03$) to a
 825 negative bias for COMBO3 ($B = -0.02$) inside both estuaries, indicating that COMBO3 performed



799 **Figure 19.** Panels (a)-(c) depict the error in the M_2 elevation amplitude solution that was computed on the COMBOx
 800 meshes. Panel (d) illustrates a CAFE plot of the error in the comparison zone for the three COMBOx meshes. Grey
 801 lines are drawn for other solutions and the S20 mesh (the best performing mesh) is indicated with an orange line.



802 **Figure 20.** A comparison of the tidal constituent root-mean-square-error (E) for the M_2 tidal elevations at 667 tidal
 803 gauge observations (c.f., Section 2.1.2) between a solution computed on the REF mesh (x-axis) and the COMBO x
 804 meshes (y-axis). The normalized bias (B) and spread (γ^2) error metrics and the total vertex (N) are indicated. Points
 805 that fall in the blue shaded region have a smaller value of E than the REF solution. Panel (a) is for the G35 solution,
 806 panel (b) for COMBO1, panel (c) for COMBO2, and panel (d) for COMBO3.



828 **Figure 21.** The complex root-mean square error (E) for the solution computed on, (a) the COMBO2 mesh, and (b)
 829 the COMBO3 mesh (includes enhanced resolution along estuarine channels), at 108 tide gauges in the Chesapeake Bay
 830 and Delaware Bay estuaries that are illustrated in panel (c). Various error metrics are indicated in the panels (a) and (b).

826 slightly better than the REF mesh here. The normalized spread of the errors γ^2 also reduced but
 827 only marginally.

831 4 Discussion and Conclusions

832 A series of controlled unstructured mesh resolution experiments conducted over a large area
 833 of ocean in high-resolution (≈ 50 m at the coast) and with a physically accurate shoreline boundary
 834 has been achieved through an automatic mesh generation approach facilitated by the *OceanMesh2D*
 835 software [Roberts *et al.*, 2018]. The sensitivity of the barotropic tidal response to unstructured
 836 mesh resolution was investigated by controlling the distribution of mesh sizes according to func-
 837 tions of *a priori* seabed and shoreline geometry information. It is noteworthy to mention that the
 838 whole process was scripted and thus automatic using the mesh generator suite. All meshes were
 839 designed to be numerically stable with a time step of 2 s without requiring post-processing hand-
 840 edits (vertex re-location, element re-shaping, or bathymetric smoothing), or *ad hoc* limiters² and
 841 dissipation attributes.

842 In coastal ocean modeling applications, the shoreline resolution determines the predominate
 843 computational expense of the model. We explored ways to quantify the effect of simplifying the

² https://wiki.adcirc.org/wiki/Fort.13_file#Elemental_Slope_Limiter

844 shoreline's representation in the mesh by coarsening the minimum resolution from 50 m to 250 m
 845 and automatically varying the resolution along the shoreline according to the width of shoreline
 846 features (Experiment 2, *feature size* function). Coarsening the minimum resolution (L_x meshes)
 847 noticeably decreased the total area of the mesh by decimating fine scale shoreline features like em-
 848 bayments, headlands, and coves leading to a reduction in the total number of vertices up to a factor
 849 of five. However, the associated variation in the tidal elevation amplitudes over most of the domain
 850 was comparatively small, the relative errors against the REF solution in 99% of the domain did not
 851 vary by more than 5%, although noticeable differences did occur in the tail of the CAFE plots cor-
 852 responding to highly localized regions. Experiment 2 demonstrated that the feature size approach
 853 FSx preserved the area enclosed by the shoreline of the mesh using the 50-m uniform shoreline
 854 resolution (see L50) while requiring approximately half the number of vertices. Further, the rela-
 855 tive errors from the REF solution for FS2 showed a significant improvement over L250 in the tail,
 856 comparable to L50.

857 An important point is that the constraints from the sizing functions interact. For example,
 858 the increase in feature size parameter from 2 to 8 improves the representation of nearshore seabed
 859 topography by using finer resolution across the width of the shoreline feature, but the higher fea-
 860 ture size parameter does not improve the ability to resolve the complexity of the shoreline as the
 861 minimum element size bound is reached (c.f. Figure 4). Thus, our recommendation is that meshes
 862 intended for high-resolution tidal modeling to be constructed with a *feature size* approach (also
 863 see *Conroy et al.* [2012]) with maximally two or three vertices across the shoreline's width instead
 864 of applying a minimum resolution uniformly along the shoreline [*Bunya et al.*, 2010; *Kerr et al.*,
 865 2013]. Note that in the feature size approach, a consideration should be taken to make sure that the
 866 element sizes along the shoreline cannot become too coarse. In this work, we applied a five-to-one
 867 ratio upper bound so that the element sizes do not exceed 250 m given that the length scales of the
 868 physical processes are still controlled by the proximity to fine scale shoreline geometry here, and
 869 coarse element sizes nearshore may not be conducive to accurately model other coastal processes
 870 that were not considered in this study such as wave setup induced through wave breaking [*Joyce*
 871 *et al.*, 2019].

872 Experiment 3 demonstrated how increasing the gradation rate can negatively impact the ap-
 873 proximation of seabed topography in the mesh and the simulated accuracy of tidal solutions were
 874 highly degraded. The mesh with the highest gradation (G35) was the worst performing mesh in
 875 terms of the M_2 and K_1 relative error values out of all 15 meshes in the five experiments. The ef-
 876 fect of increasing the gradation is likely to have increased the numerical error [*Hagen et al.*, 2000]
 877 in addition to the physical domain approximation error (e.g., representation of seabed topography)
 878 making the determination of the root cause of the poor performance challenging. However, experi-
 879 ment 4 clearly demonstrated that placing resolution along seabed gradients (~ 1 km along the conti-
 880 nental shelf break and slope) improved the accuracy of tidal solutions, which is in agreement with
 881 prior works [*Luettich and Westerink*, 1995; *Chen et al.*, 2016]. At the same time, increasing the gra-
 882 dation rate coarsened the representation of the continental shelf break as resolution sizes would
 883 grow faster from the shoreline. Thus, it is likely that our application of resolution along seabed
 884 gradients reduces the numerical error as large gradients in the solution are co-located with steep
 885 seabed topographic gradients [e.g., *Hannah and Wright*, 1995; *Hagen et al.*, 2001]. Our recommen-
 886 dation is the use of a high value for the slope mesh size function (e.g., S10-S20) in combination
 887 with a high gradation rate (e.g., G35) to offset the negative impacts on both error sources, while
 888 largely reducing the total number of vertices in the mesh.

889 Experiment 5 demonstrated that the approximation of the seabed topography across estuaries
 890 with deep-draft channels (e.g., Chesapeake Bay and Delaware Bay) could be improved by using
 891 the *estuarine channel* mesh size function to place targeted high-resolution zones along the subma-
 892 rine channels inside and leading into estuaries. In estuaries that are characterized by well-defined
 893 submarine channels that occupy non-trivial portions of the width of the estuary, it is important to
 894 ensure that adequate resolution is placed along these channels so that the total cross-sectional area
 895 and local ocean depth minima are preserved. Indeed, progressively placing finer mesh resolution
 896 along the estuarine channel network (extracted using an upslope area computation on the DEM)

897 was shown to reduce tidal error metrics as compared to both the reference solution and measured
 898 data as inland waterway conveyances are improved and frictional resistance is reduced. We remark
 899 that other mesh size heuristics, such as the slope mesh size function and using finer resolution
 900 along the shoreline with a low gradation rate can implicitly, but inefficiently, capture these sub-
 901 marine channel features. Thus, the application of the *estuarine channel* mesh size function allows
 902 the usage of a higher mesh size gradation so as to focus resolution only on the submarine channels
 903 allowing us to more efficiently discretize the estuarine environment.

904 We tested the performance of mesh design strategies that involved using a steep mesh size
 905 gradation rate (G35) in combination with the targeted mesh sizing functions along the shoreline
 906 (FSx), sharp topographic gradients (Sx), and estuarine channel systems (Cx). Three combination
 907 meshes (COMBOx) that ranged from 1.1 million to 2.3 million vertices were generated. Over-
 908 all, all COMBOx meshes performed similarly to the REF mesh both directly and as compared to
 909 measured tide gauge data. The additive effects of multiple mesh size functions reduced the error
 910 metrics largely, especially in the comparison to the G35 solution, which had a noticeably degraded
 911 solution without the usage of other sizing functions (in particular the *slope* function) used in the
 912 COMBOx sequence.

913 Echoing our findings from Experiment 1, the COMBO2 mesh utilized a small value of the
 914 *feature size* function parameter (FS2) and had approximately half the vertex count of COMBO1
 915 (uniform shoreline resolution) with little increase in relative error, thus the FS2 is considered an
 916 efficient mesh design choice. However, deep-draft channels within estuarine are more likely to
 917 poorly represented with the high gradation (G35) and FSx design combination as mesh sizes will
 918 become coarser in certain regions depending on the cusped shape of the shoreline. Our conclu-
 919 sion is the 15% increase in the total vertex count associated with the addition of the C0.5 com-
 920 ponent of COMBO3 to better capture estuarine channels, can be considered a good investment
 921 particularly since the solution in nearshore estuaries of high importance is improved; even to a
 922 point beyond the performance of the REF mesh (e.g., Figure 21). Our results imply that the 250-m
 923 bounded blanket resolution applied across the large estuaries in reference solution is coarser and
 924 less effective than the targeted resolution that follows the channelized seabed in the C0.5 mesh
 925 size function. In fact, a key drawback of mesh designs that apply uniformly fine zones of resolu-
 926 tion throughout regions of similar ocean depths (the wavelength-to-gridscale heuristic [e.g., *West-
 927 erink et al.*, 1994] is that there is less flexibility to more finely capture targeted seabed features and
 928 shoreline constrictions due to the baseline expense of the model. In many regions, the application
 929 of targeted refinement can produce more finely resolved solutions in localized areas of importance
 930 with far fewer vertices.

931 Through the combination of the constraints imposed by a set of mesh size functions (COMBOx
 932 meshes), the vertex count was reduced by nearly an order of magnitude from the reference mesh
 933 and had a converged solution with tidal error metrics in 99% of the East and Gulf Coast waters
 934 ranging from -2% to +1%. For instance COMBO3 (1.3 million vertices) had eight times fewer ver-
 935 tices as the reference (10.8 million vertices). These results suggest that pre-existing operational
 936 models may be largely inefficient, over-discretizing in some areas and under-discretizing in oth-
 937 ers as pre-existing models use nearly uniform resolution nearshore and land and following the
 938 wavelength-to-gridscale sizing heuristic offshore. For example, the Hurricane Surge Operational
 939 Forecasting system (HSOFS) mesh [*Technology Riverside Inc. and AECOM*, 2015] used in real-
 940 time predictions employs a minimum shoreline resolution of 250 m and contains 0.75 million un-
 941 derwater vertices, which is similar in number to our L250 mesh. In contrast, the COMBO3 mesh,
 942 which spans the same ECGC study region, utilizes up to five times finer resolution nearshore (50
 943 m compared to 250 m) and up to ten times finer resolution along the continental slope (1 km com-
 944 pared to 10 km), with only 1.6 times the total number of underwater vertices than HSOFS.

945 We highlight that an important first step in the coastal model development procedure is to
 946 construct a mesh that minimizes the physical domain approximation error before model tuning oc-
 947 curs *vis-a-vis* varying bottom friction, other dissipative coefficients, viscous models, and manually
 948 altering ocean depths and shoreline form. As was evident in this paper, by improving the accu-
 949 racy of the approximate problem (i.e., the representation of the shoreline and seabed topography

as per the available geospatial data used), the tidal solutions exhibited convergence towards a reference solution. The primary variation in the M_2 (c.f., Figure 16) tended to coincide with zones of the ECGC in which the bottom friction coefficient are typically modified [Szpilka et al., 2016]. For instance, since the Chesapeake Bay has a muddy seabed floor, the friction coefficient, C_f is often set low a value ($C_f \approx 0.001$) and this is found to improve comparisons with tidal harmonics [Friedrichs, 2010]. However, our results indicate that the the M_2 tide in the Chesapeake estuary is largely sensitive to mesh design with changes around 15% between the mesh design variations explored here (c.f., Figure 16). It is thus likely that the bottom friction application procedure may be tuned incorrectly depending on the local mesh design; for instance, depending on the complexity of the estuarine network in the mesh.

This study highlights the need to perform convergence studies to determine the role of mesh resolution on solutions of coastal hydrodynamics. We have provided a framework to perform these convergence studies and also suggestions for starting mesh size function parameters (e.g., COMBO3) and the effect they have on the solution of surface tides.

Acknowledgments

This work was supported by the Joseph and Nona Ahearn endowment at the University of Notre Dame and was completed under USDOC NOAA Award NA18OAR4590377. *OceanMesh2D* V2.0 is available from <https://doi.org/10.5281/zenodo.2560555>.

References

- Amante, C., and B. Eakins (2009), ETOPO1 1 Arc-Minute Global Relief Model: Procedures, Data Sources and Analysis. NOAA Technical Memorandum NESDIS NGDC-24. National Geophysical Data Center, NOAA., doi:10.7289/V5C8276M.
- Avdis, A., A. S. Candy, J. Hill, S. C. Kramer, and M. D. Piggott (2018), Efficient unstructured mesh generation for marine renewable energy applications, *Renewable Energy*, 116, 842 – 856, doi:10.1016/j.renene.2017.09.058.
- Bacopoulos, P., and S. C. Hagen (2017), The intertidal zones of the south atlantic bight and their local and regional influence on astronomical tides, *Ocean Modelling*, 119, 13 – 34, doi:10.1016/j.ocemod.2017.09.002.
- Beardsley, R. C., C. Chen, and Q. Xu (2013), Coastal flooding in Scituate (MA): A FVCOM study of the 27 December 2010 nor'easter, *Journal of Geophysical Research: Oceans*, 118(11), 6030–6045, doi:10.1002/2013JC008862.
- Behrens, J. (1998), Atmospheric and ocean modeling with an adaptive finite element solver for the shallow-water equations, *Applied Numerical Mathematics*, 26(1), 217 – 226, doi:10.1016/S0168-9274(97)00090-1.
- Bilgili, A., K. W. Smith, and D. R. Lynch (2006), BatTri: A two-dimensional bathymetry-based unstructured triangular grid generator for finite element circulation modeling, *Computers and Geosciences*, 32(5), 632–642, doi:10.1016/j.cageo.2005.09.007.
- Blain, C. A., J. J. Westerink, and R. A. Luettich (1998), Grid convergence studies for the prediction of hurricane storm surge, *International Journal for Numerical Methods in Fluids*, 26(4), 369–401, doi:10.1002/(SICI)1097-0363(19980228)26:4<369::AID-FLD624>3.0.CO;2-0.
- Blanton, B. O., F. E. Werner, H. E. Seim, R. A. Luettich, D. R. Lynch, K. W. Smith, G. Voulgaris, F. M. Bingham, and F. Way (2004), Barotropic tides in the South Atlantic Bight, *Journal of Geophysical Research C: Oceans*, 109(12), 1–17, doi:10.1029/2004JC002455.
- Bunya, S., J. C. Dietrich, J. J. Westerink, B. A. Ebersole, J. M. Smith, J. H. Atkinson, R. Jensen, D. T. Resio, R. A. Luettich, C. Dawson, V. J. Cardone, A. T. Cox, M. D. Powell, H. J. Westerink, and H. J. Roberts (2010), A High-Resolution Coupled Riverine Flow, Tide, Wind, Wind Wave, and Storm Surge Model for Southern Louisiana and Mississippi. Part I: Model Development and Validation, *Monthly Weather Review*, 138(2), 345–377, doi:10.1175/2009MWR2906.1.
- Candy, A., and J. Pietrzak (2018), Shingle 2.0: Generalising self-consistent and automated domain discretisation for multi-scale geophysical models, *Geoscientific Model Development*, pp. 213–

- 234, doi:10.5194/gmd-11-213-2018.
- 1000
1001 Chen, C., H. Huang, R. C. Beardsley, Q. Xu, R. Limeburner, G. W. Cowles, Y. Sun, J. Qi, and
1002 H. Lin (2011), Tidal dynamics in the Gulf of Maine and New England Shelf: An application of
1003 FVCOM, *Journal of Geophysical Research: Oceans*, *116*(12), 1–14, doi:10.1029/2011JC007054.
- 1004 Chen, C., R. C. Beardsley, R. A. Luettich, J. J. Westerink, H. Wang, W. Perrie, Q. Xu, A. S. Don-
1005 ahue, J. Qi, H. Lin, L. Zhao, P. C. Kerr, Y. Meng, and B. Toulany (2013), Extratropical storm
1006 inundation testbed: Intermodel comparisons in Scituate, Massachusetts, *Journal of Geophysical
1007 Research: Oceans*, *118*(10), 5054–5073, doi:10.1002/jgrc.20397.
- 1008 Chen, C., G. Gao, Y. Zhang, R. C. Beardsley, Z. Lai, J. Qi, and H. Lin (2016), Circulation in the
1009 Arctic Ocean: Results from a high-resolution coupled ice-sea nested Global-FVCOM and Arctic-
1010 FVCOM system, *Progress in Oceanography*, *141*, 60–80, doi:10.1016/j.pocean.2015.12.002.
- 1011 Clarke, A. J., and D. S. Battisti (1981), The effect of continental shelves on tides, *Deep Sea Re-
1012 search Part A. Oceanographic Research Papers*, *28*(7), 665 – 682, doi:10.1016/0198-0149(81)
1013 90128-X.
- 1014 Conroy, C. J., E. J. Kubatko, and D. W. West (2012), ADMESH: An advanced, automatic unstruc-
1015 tured mesh generator for shallow water models, *Ocean Dynamics*, *62*(10-12), 1503–1517, doi:
1016 10.1007/s10236-012-0574-0.
- 1017 Cyriac, R., J. Dietrich, J. Fleming, B. Blanton, C. Kaiser, C. Dawson, and R. Luettich (2018), Vari-
1018 ability in Coastal Flooding predictions due to forecast errors during Hurricane Arthur, *Coastal
1019 Engineering*, *137*, 59 – 78, doi:10.1016/j.coastaleng.2018.02.008.
- 1020 Dietrich, J. C., S. Bunya, J. J. Westerink, B. A. Ebersole, J. M. Smith, J. H. Atkinson, R. Jensen,
1021 D. T. Resio, R. A. Luettich, C. Dawson, V. J. Cardone, A. T. Cox, M. D. Powell, H. J. West-
1022 erink, and H. J. Roberts (2010), A High-Resolution Coupled Riverine Flow, Tide, Wind, Wind
1023 Wave, and Storm Surge Model for Southern Louisiana and Mississippi. Part II: Synoptic De-
1024 scription and Analysis of Hurricanes Katrina and Rita, *Monthly Weather Review*, *138*(2), 378–
1025 404, doi:10.1175/2009MWR2907.1.
- 1026 Dietrich, J. C., J. J. Westerink, A. B. Kennedy, J. M. Smith, R. E. Jensen, M. Zijlema, L. H.
1027 Holthuijsen, C. Dawson, R. A. Luettich, M. D. Powell, V. J. Cardone, A. T. Cox, G. W. Stone,
1028 H. Pourtaheri, M. E. Hope, S. Tanaka, L. G. Westerink, H. J. Westerink, and Z. Cobell (2011),
1029 Hurricane gustav (2008) waves and storm surge: Hindcast, synoptic analysis, and validation in
1030 southern louisiana, *Monthly Weather Review*, *139*(8), 2488–2522, doi:10.1175/2011MWR3611.1.
- 1031 Dronkers, J. (1986), Tidal asymmetry and estuarine morphology, *Netherlands Journal of Sea Re-
1032 search*, *20*(2), 117 – 131, doi:10.1016/0077-7579(86)90036-0.
- 1033 Engwirda, D. (2014), Locally optimal Delaunay-refinement and optimisation-based mesh genera-
1034 tion, Ph.D. thesis, University of Sydney.
- 1035 Engwirda, D. (2017), JIGSAW-GEO (1.0): Locally orthogonal staggered unstructured grid genera-
1036 tion for general circulation modelling on the sphere, *Geoscientific Model Development*, *10*(6),
1037 2117–2140, doi:10.5194/gmd-10-2117-2017.
- 1038 Fleming, J. G., C. W. Fulcher, R. a. Luettich, B. D. Estrade, G. D. Allen, and H. S. Winer (2008),
1039 A Real Time Storm Surge Forecasting System Using ADCIRC, in *10th International Confer-
1040 ence on Estuarine and Coastal Modeling*, pp. 893–912, Newport, Rhode Island, doi:10.1061/
1041 40990(324)48.
- 1042 Friedrichs, C. T. (2010), Barotropic tides in channelized estuaries, in *Contemporary Issues in Es-
1043 tuarine Physics*, edited by A. Valle-Levinson, pp. 27–61, Cambridge University Press, doi:
1044 10.1017/CBO9780511676567.004.
- 1045 Garrett, C., and E. Kunze (2007), Internal Tide Generation in the Deep Ocean, *Annual Review of
1046 Fluid Mechanics*, *39*(1), 57–87, doi:10.1146/annurev.fluid.39.050905.110227.
- 1047 Gorman, G., M. Piggott, M. Wells, C. Pain, and P. Allison (2008), A systematic approach to un-
1048 structured mesh generation for ocean modelling using gmt and terreno, *Computers and Geo-
1049 sciences*, *34*(12), 1721–1731, doi:10.1016/j.cageo.2007.06.014.
- 1050 GRASS Development Team (2017), *Geographic Resources Analysis Support System (GRASS GIS)
1051 Software, Version 7.2*, Open Source Geospatial Foundation.
- 1052 Green, J. A. M., and J. Nycander (2013), A Comparison of Tidal Conversion Parameterizations for
1053 Tidal Models, *Journal of Physical Oceanography*, *43*(1), 104–119, doi:10.1175/JPO-D-12-023.1.

- 1054 Greenberg, D. A., F. Dupont, F. H. Lyard, D. R. Lynch, and F. E. Werner (2007), Resolution issues
1055 in numerical models of oceanic and coastal circulation, *Continental Shelf Research*, 27(9), 1317–
1056 1343, doi:10.1016/j.csr.2007.01.023.
- 1057 Hagen, S. C., J. J. Westerink, and R. L. Kolar (2000), One-dimensional finite element grids based
1058 on a localized truncation error analysis, *International Journal for numerical methods in fluids*, 32,
1059 241–261, doi:10.1002/(SICI)1097-0363(20000130)32:2<241::AID-FLD947>3.0.CO;2-{\#}.
- 1060 Hagen, S. C., J. J. Westerink, R. L. Kolar, and O. Horstmann (2001), Two-dimensional, unstruc-
1061 tured mesh generation for tidal models, *International Journal for Numerical Methods in Fluids*,
1062 35(6), 669–686, doi:10.1002/1097-0363(20010330)35:6<669::AID-FLD108>3.0.CO;2-{\#}.
- 1063 Hagen, S. C., O. Horstmann, and R. J. Bennett (2002), An unstructured mesh generation algorithm
1064 for shallow water modeling, *International Journal of Computational Fluid Dynamics*, 16(2), 83–
1065 91, doi:10.1080/10618560290017176.
- 1066 Hannah, C., and D. Wright (1995), Depth dependent analytical and numerical solutions for wind-
1067 driven flow in the coastal ocean, *Quantitative Skill Assessment for Coastal Ocean Models*, 47,
1068 125–152.
- 1069 Hendershott, M. C. (1972), The Effects of Solid Earth Deformation on Global Ocean Tides, *Geo-
1070 physical Journal International*, 29(4), 389–402, doi:10.1111/j.1365-246X.1972.tb06167.x.
- 1071 Hope, M. E., J. J. Westerink, A. B. Kennedy, P. C. Kerr, J. C. Dietrich, C. Dawson, C. J. Bender,
1072 J. M. Smith, R. E. Jensen, M. Zijlema, L. H. Holthuijsen, R. A. Luettich, M. D. Powell, V. J.
1073 Cardone, A. T. Cox, H. Pourtaheri, H. J. Roberts, J. H. Atkinson, S. Tanaka, H. J. Westerink,
1074 and L. G. Westerink (2013), Hindcast and validation of Hurricane Ike (2008) waves, forerunner,
1075 and storm surge, *Journal of Geophysical Research: Oceans*, 118(9), 4424–4460, doi:10.1002/jgrc.
1076 20314.
- 1077 Huthnance, J. M. (1995), Circulation, exchange and water masses at the ocean margin: the role of
1078 physical processes at the shelf edge, *Progress in Oceanography*, 35(4), 353 – 431, doi:10.1016/
1079 0079-6611(95)80003-C.
- 1080 Joyce, B., J. Gonzalez-Lopez, A. J. van der Westhuysen, D. Yang, W. J. Pringle, J. J. Westerink,
1081 and A. T. Cox (2019), U.S. IOOS Coastal and Ocean Modeling Testbed: Hurricane-induced
1082 Winds, Waves and Surge for Deep-ocean, Reef Fringed Islands in the Caribbean, *Journal of Geo-
1083 physical Research C: Oceans*, doi:10.1029/2018JC014687.
- 1084 Kerr, P. C., R. C. Martyr, A. S. Donahue, M. E. Hope, J. J. Westerink, R. A. Luettich, A. B.
1085 Kennedy, J. C. Dietrich, C. Dawson, and H. J. Westerink (2013), U.S. IOOS coastal and ocean
1086 modeling testbed: Evaluation of tide, wave, and hurricane surge response sensitivities to mesh
1087 resolution and friction in the Gulf of Mexico, *Journal of Geophysical Research: Oceans*, 118(9),
1088 4633–4661, doi:10.1002/jgrc.20305.
- 1089 Kinnmark, I. (1988), The shallow water wave equations: Formulation, analysis and application,
1090 *SIAM Review*, 30(3), 517–518, doi:10.1137/1030116.
- 1091 Loder, J. W. (1980), Topographic Rectification of Tidal Currents on the Sides of Georges Bank,
1092 *Journal of Physical Oceanography*, 10(9), 1399–1416, doi:10.1175/1520-0485(1980)010<1399:
1093 TROTCO>2.0.CO;2.
- 1094 Luettich, R., and J. J. Westerink (2004), Formulation and Numerical Implementation of the 2D/3D
1095 ADCIRC Finite Element Model Version 44.XX, *Tech. rep.*
- 1096 Luettich, R., Jr, and J. J. Westerink (1995), Continental Shelf Scale Convergence Studies with a
1097 Barotropic Tidal Model, *Quantitative Skill Assessment for Coastal Ocean Models, A.G.U.*, 47, doi:
1098 10.1029/CE047p0349.
- 1099 Luettich, R. A., and J. J. Westerink (2013), *Continental Shelf Scale Convergence Studies with a
1100 Barotropic Tidal Model*, chap. 16, pp. 349–371, American Geophysical Union (AGU), doi:
1101 10.1029/CE047p0349.
- 1102 Lyard, F., F. Lefevre, T. Letellier, and O. Francis (2006), Modelling the global ocean tides: modern
1103 insights from FES2004, *Ocean Dynamics*, 56(5-6), 394–415, doi:10.1007/s10236-006-0086-x.
- 1104 Lynch, D. R., and W. G. Gray (1979), A wave equation model for finite element tidal computa-
1105 tions, *Computers Fluids*, 7(3), 207 – 228, doi:10.1016/0045-7930(79)90037-9.
- 1106 Marsooli, R., and N. Lin (2018), Numerical Modeling of Historical Storm Tides and Waves and
1107 Their Interactions Along the U.S. East and Gulf Coasts, *Journal of Geophysical Research:*

- 1108 *Oceans*, pp. 3844–3874, doi:10.1029/2017JC013434.
- 1109 Massey, T. C. (2015), Locally constrained nodal connectivity refinement procedures for unstruc-
 1110 tured triangular finite element meshes, *Engineering with Computers*, 31(2), 375–386, doi:
 1111 10.1007/s00366-014-0357-y.
- 1112 Molines, J., M. Fornerino, and C. L. Provost (1989), Tidal spectroscopy of a coastal area: observed
 1113 and simulated tides of the lake maracaibo system, *Continental Shelf Research*, 9(4), 301 – 323,
 1114 doi:10.1016/0278-4343(89)90036-8.
- 1115 Muis, S., N. Lin, M. Verlaan, H. C. Winsemius, P. J. Ward, and J. C. J. H. Aerts (2019), Spa-
 1116 tiotemporal patterns of extreme sea levels along the western North-Atlantic coasts, *Scientific*
 1117 *Reports*, 9(1), 3391, doi:10.1038/s41598-019-40157-w.
- 1118 Oden, J., L. Demkowicz, W. Rachowicz, and T. Westermann (1990), A posteriori error analysis in
 1119 finite elements: The element residual method for symmetrizable problems with applications to
 1120 compressible euler and navier-stokes equations, *Computer Methods in Applied Mechanics and En-*
 1121 *gineering*, 82(1), 183 – 203, doi:10.1016/0045-7825(90)90164-H, proceedings of the Workshop
 1122 on Reliability in Computational Mechanics.
- 1123 Parker, B. B. (1991), The relative importance of the various nonlinear mechanisms in a wide range
 1124 of tidal interactions (Review), in *Tidal hydrodynamics*, edited by B. B. Parker, pp. 237–268, John
 1125 Wiley & Sons, Inc., New York, USA.
- 1126 Parrish, D. M., and S. C. Hagen (2009), Incorporating spatially variable bottom stress and Coriolis
 1127 force into 2D, a posteriori , unstructured mesh generation for shallow water models, *Interna-*
 1128 *tional Journal for Numerical Methods in Fluids*, 60(3), 237–261, doi:10.1002/flid.1882.
- 1129 Pawlowicz, R. (2018), M_Map: A mapping package for MATLAB, version 1.4j, www.eoas.ubc.ca/~rich/map.html.
- 1130
- 1131 Persson, P. O. (2006), Mesh size functions for implicit geometries and PDE-based gradient limit-
 1132 ing, *Engineering with Computers*, 22(2), 95–109, doi:10.1007/s00366-006-0014-1.
- 1133 Prandle, D. (2003), Relationships between tidal dynamics and bathymetry in strongly convergent
 1134 estuaries, *Journal of Physical Oceanography*, 33(12), 2738–2750, doi:10.1175/1520-0485(2003)
 1135 033<2738:RBTDAB>2.0.CO;2.
- 1136 Pringle, W. J., D. Wirasaet, A. Suhardjo, J. Meixner, J. J. Westerink, A. B. Kennedy, and S. Nong
 1137 (2018a), Finite-Element Barotropic Model for the Indian and Western Pacific Oceans: Tidal
 1138 Model-Data Comparisons and Sensitivities, *Ocean Modelling*, 129, 13–38, doi:10.1016/j.ocemod.
 1139 2018.07.003.
- 1140 Pringle, W. J., D. Wirasaet, and J. J. Westerink (2018b), Modifications to Internal Tide Conversion
 1141 Parameterizations and Implementation into Barotropic Ocean Models, *EarthArXiv*, p. 9, doi:10.
 1142 31223/osf.io/84w53.
- 1143 Pringle, W. J., J. Gonzalez-lopez, B. Joyce, J. J. Westerink, and A. J. van der Westhuysen (2019),
 1144 Baroclinic Coupling Improves Depth-Integrated Modeling of Coastal Sea Level Variations
 1145 around Puerto Rico and the U.S . Virgin Islands, *Journal of Geophysical Research: Oceans*, doi:
 1146 10.1029/2018JC014682.
- 1147 Remacle, J.-F., and J. Lambrechts (2016), Fast and Robust Mesh Generation on the Sphere - Appli-
 1148 cation to Coastal Domains, *Procedia Engineering*, 163, 20–32, doi:10.1016/j.proeng.2016.11.011.
- 1149 Roache, P. J. (1994), Perspective: A Method for Uniform Reporting of Grid Refinement Studies,
 1150 *Journal of Fluids Engineering*, 116(3), 405, doi:10.1115/1.2910291.
- 1151 Roberts, K. J., and W. J. Pringle (2018), OceanMesh2D: User guide - Precise distance-based
 1152 two-dimensional automated mesh generation, *Tech. Rep. June*, University of Notre Dame, doi:
 1153 10.13140/RG.2.2.21840.61446/1.
- 1154 Roberts, K. J., W. J. Pringle, and J. J. Westerink (2018), OceanMesh2D 1.0: MATLAB-based soft-
 1155 ware for two-dimensional unstructured mesh generation in coastal ocean modeling, *Geoscientific*
 1156 *Model Development Discussions*, p. in review, doi:10.5194/gmd-2018-203.
- 1157 Sandwell, D. T., J. J. Becker, C. Olson, and A. Jackson (2014), SRTM15_PLUS: Data Fusion of
 1158 SRTM Land Topography with Measured and Estimated Seafloor topography.
- 1159 Shewchuk, J. R. (2002), What is a good linear finite element? - interpolation, conditioning,
 1160 anisotropy, and quality measures, *Tech. rep.*, In Proc. of the 11th International Meshing
 1161 Roundtable.

- 1162 Stammer, D., R. D. Ray, O. B. Andersen, B. K. Arbic, W. Bosch, L. Carrère, Y. Cheng, D. S.
1163 Chinn, B. D. Dushaw, G. D. Egbert, S. Y. Erofeeva, H. S. Fok, J. A. M. Green, S. Griffiths,
1164 M. A. King, V. Lapin, F. G. Lemoine, S. B. Luthcke, F. Lyard, J. Morison, M. Müller, L. Pad-
1165 man, J. G. Richman, J. F. Shriver, C. K. Shum, E. Taguchi, and Y. Yi (2014), Accuracy as-
1166 sessment of global barotropic ocean tide models, *Reviews of Geophysics*, 52(3), 243–282, doi:
1167 10.1002/2014RG000450.
- 1168 Szpilka, C., K. Dresback, R. Kolar, J. Feyen, and J. Wang (2016), Improvements for the Western
1169 North Atlantic, Caribbean and Gulf of Mexico ADCIRC Tidal Database (EC2015), *Journal of*
1170 *Marine Science and Engineering*, 4(4), doi:10.3390/jmse4040072.
- 1171 Tanaka, S., S. Bunya, J. J. Westerink, C. Dawson, and R. A. Luettich (2011), Scalability of an Un-
1172 structured Grid Continuous Galerkin Based Hurricane Storm Surge Model, *Journal of Scientific*
1173 *Computing*, 46(3), 329–358, doi:10.1007/s10915-010-9402-1.
- 1174 Technology Riverside Inc., and AECOM (2015), Mesh Development, Tidal Validation, and Hind-
1175 cast Skill Assessment of an ADCIRC Model for the Hurricane Storm Surge Operational Forecast
1176 System on the US Gulf-Atlantic Coast, *Tech. rep.*, National Oceanic and Atmospheric Admin-
1177 istration/Nation Ocean Service, Coast Survey Development Laboratory, Office of Coast Survey,
1178 doi:10.7921/GOMC8X6V.
- 1179 Westerink, J. J., R. A. Luettich, A. M. Baptists, N. W. Scheffner, and P. Farrar (1992), Tide
1180 and Storm Surge Predictions Using Finite Element Model, *Journal of Hydraulic Engineering*,
1181 118(10), 1373–1390, doi:10.1061/(ASCE)0733-9429(1992)118:10(1373).
- 1182 Westerink, J. J., L. R. A., and M. J. C. (1994), Modelling tides in the western North Atlantic using
1183 unstructured graded grids, *Tellus A*, 46(2), 178–199, doi:10.1034/j.1600-0870.1994.00007.x.
- 1184 Westerink, J. J., R. A. Luettich, J. C. Feyen, J. H. Atkinson, C. Dawson, H. J. Roberts, M. D.
1185 Powell, J. P. Dunion, E. J. Kubatko, and H. Pourtaheri (2008), A Basin- to Channel-Scale Un-
1186 structured Grid Hurricane Storm Surge Model Applied to Southern Louisiana, *Monthly Weather*
1187 *Review*, 136(3), 833–864, doi:10.1175/2007MWR1946.1.
- 1188 White, S., and K. Hess (2016), An Assessment of the Revised VDatum for Eastern Florida, Geor-
1189 gia, South Carolina, and North Carolina. NOAA Technical Memorandum NOS CS 38.
- 1190 Xie, D.-m., Q.-p. Zou, and J. W. Cannon (2016), Application of SWAN+ADCIRC to tide-surge
1191 and wave simulation in Gulf of Maine during Patriot’s Day storm, *Water Science and Engineer-*
1192 *ing*, 9(1), 33–41, doi:10.1016/j.wse.2016.02.003.
- 1193 Xing, J., and A. M. Davies (1998), A three-dimensional model of internal tides on the Malin-
1194 Hebrides shelf and shelf edge, *Journal of Geophysical Research: Oceans*, 103(C12), 27,821–
1195 27,847, doi:10.1029/98JC02149.
- 1196 Xu, Q., C. Chen, J. Qi, H. Lin, R. C. Beardsley, and Y. Sun (2013), Impact of current-wave in-
1197 teraction on storm surge simulation: A case study for Hurricane Bob, *Journal of Geophysical*
1198 *Research: Oceans*, 118(5), 2685–2701, doi:10.1002/jgrc.20207.
- 1199 Zhang, Y., and A. M. Baptista (2008), SELFE: A semi-implicit Eulerian-Lagrangian finite-element
1200 model for cross-scale ocean circulation, *Ocean Modelling*, 21(3-4), 71–96, doi:10.1016/j.ocemod.
1201 2007.11.005.
- 1202 Zhang, Y. J., F. Ye, E. V. Stanev, and S. Grashorn (2016), Seamless cross-scale modeling with
1203 SCHISM, *Ocean Modelling*, 102, 64–81, doi:10.1016/j.ocemod.2016.05.002.
- 1204 Zheng, L., R. H. Weisberg, Y. Huang, R. A. Luettich, J. J. Westerink, P. C. Kerr, A. S. Donahue,
1205 G. Crane, and L. Akli (2013), Implications from the comparisons between two- and three- di-
1206 mensional model simulations of the Hurricane Ike storm surge, *Journal of Geophysical Research*
1207 *C: Oceans*, 118, 3350–3369, doi:10.1002/jgrc.20248.